

Peer-Reviewed Technical Communication

INS/GPS Aided by Frequency Contents of Vector Observations With Application to Autonomous Surface Crafts

J. F. Vasconcelos, *Member, IEEE*, C. Silvestre, *Member, IEEE*, and P. Oliveira, *Member, IEEE*

Abstract—This paper presents a high-accuracy, multirate inertial navigation system (INS) integrating global positioning system (GPS) measurements and advanced vector aiding techniques for precise position and attitude estimation of autonomous surface crafts (ASCs). Designed to be implemented and tested in the DELFIMx catamaran developed at ISR/IST, the navigation system comprises an advanced inertial integration algorithm to account for coning and sculling motions, combined with an extended Kalman filter (EKF) for inertial sensor error compensation. Aiding gravitational observations are optimally exploited in the EKF, by deriving a sensor integration technique that takes into account the vehicle's dynamics bandwidth information to properly trace measurement disturbances and extract the relevant sensor information. The proposed aiding technique and the performance of the navigation system are assessed using experimental data obtained at seatrials with a low-cost hardware architecture installed on-board the DELFIMx platform. It is shown that the low frequency information embodied in pendular measurements improves the compensation of inertial sensor bias and noise, and consequently enhances the performance of position and attitude estimation. The overall improvements obtained with the vector aiding observations are also illustrated for the case of GPS signal outage, emphasizing the extended autonomy of the navigation system with respect to position aiding.

Index Terms—Inertial navigation, Kalman filtering, autonomous vehicles, marine technology.

I. INTRODUCTION

AUTONOMOUS SURFACE CRAFTS (ASCs) are versatile robotic platforms, capable of performing a wide and valuable range of operational tasks in challenging scenarios. Applications of interest for the civilian community include the inspection of coastal areas and the maintenance of large critical semisubmerged infrastructures like bridges and breakwaters, that in general require complex and expensive routine inspection procedures. Most of these structures are exposed

Manuscript received November 12, 2008; revised January 18, 2011; accepted March 02, 2011. Date of current version May 27, 2011. This work was supported in part by Fundação para a Ciência e a Tecnologia (ISR/IST plurianual funding) through the POS_Conhecimento Program that includes FEDER funds and by the project MEDIREs from ADI and project PDCT/MAR/55609/2004-RUMOS of the FCT. The work of J. F. Vasconcelos was supported by the Ph.D. Student Scholarships SFRH/BD/18954/2004 from the Portuguese FCT POCTI programme.

Associate Editors: B. Calder and C. De Moustier.

The authors are with the Institute for Systems and Robotics (ISR), Instituto Superior Técnico, Lisbon, Portugal (e-mails: jfvasconcelos@isr.ist.utl.pt; cjs@isr.ist.utl.pt; pjcro@isr.ist.utl.pt).

Color versions of one or more of the figures in this paper are available online at <http://ieeexplore.ieee.org>.

Digital Object Identifier 10.1109/JOE.2011.2126170



Fig. 1. The DELFIMx autonomous surface craft. The catamaran is 4.5 m long and 2.45 m wide, with a mass of 300 Kg. Propulsion is ensured by two propellers driven by electrical motors, and the maximum rated speed of the vehicle with respect to the water is 6 kn.

to harsh environments and heavy loads and some of them are designed under the proviso that maintenance work will be required during the structure's life. Performance specifications often demand ultra light weight, high performance, robust navigation systems to provide high-resolution position and attitude estimates that characterize accurately the infrastructure status [1], while compensating for the influence of the vehicle motion on the data acquired by the sonars and the LIDAR. However, adopted low-cost sensor units are affected by nonidealities that hinder the required accuracy, and call for advanced filtering techniques that make use of the measurement redundancy and exploit the available information about the kinematics and dynamics of the vehicle. This motivates the autonomous vehicles scientific community to develop high accuracy algorithms for strapdown navigation systems, merging the available sensor data, and compensating for disturbances such as bias and noise.

The autonomous catamaran DELFIMx, an ASC built at Institute for Systems and Robotics, Instituto Superior Técnico (ISR/IST), and displayed in Fig. 1, was designed for automatic marine data acquisition for risk assessment in semisubmerged structures [2]. This robotic platform allows for the access to remote and confined locations in a systematic way, as required for precise sonar and LIDAR data acquisition. To successfully execute its mission, the ASC is required to have a reliable on-board navigation system based on low-power consumption, inexpensive hardware, capable of efficiently integrating the information from inertial and aiding sensor suites. The problem of poor GPS signal detection due to the proximity to the surveyed structure also demands for a navigation system able to operate under medium term position aiding shortage.

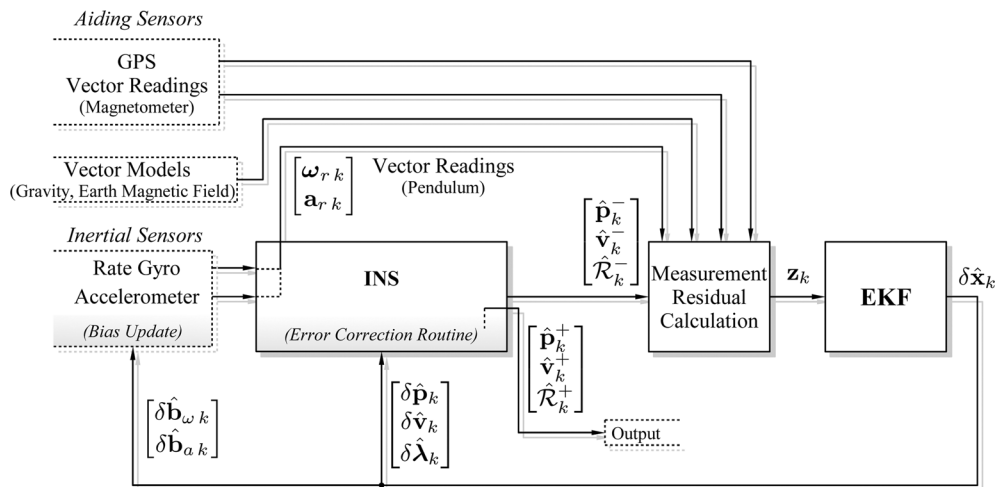


Fig. 2. Navigation system block diagram: the INS block integrates the inertial sensor data to produce attitude, velocity, and position estimates; the EKF merges the aiding sensor information and the INS estimates, to dynamically compute the inertial estimation errors; the error correction routines integrate the error estimates provided by EKF in the inertial system.

This paper describes the design and implementation of a navigation system with application to autonomous vehicles. The main contributions of this work are 1) to provide a tutorial description of the design of a high-accuracy, low cost navigation system, encompassing a high-accuracy multirate inertial integration algorithm, 2) to propose a sensor integration method that takes the vehicle's dynamic into consideration and that improves position and attitude estimates for critical maneuvers, and 3) to validate the proposed navigation system and sensor integration with experimental data containing modeled and unmodeled real disturbances.

In this work, a multirate, high-accuracy inertial navigation system (INS) integration algorithm is adopted to compute attitude, velocity and position, and is combined with an extended Kalman filter (EKF) to integrate GPS position measurements, vector observations and frequency domain characterization of the vehicle. Magnetic and gravitational observations are integrated optimally in the EKF, by modeling the sensor readings directly in the filter and by taking into account the vehicle's dynamics bandwidth information. More concretely, this paper develops a technique to model pendular measurements in the frequency domain, to exclude the influence of linear accelerations, and validates the proposed approach in simulation and experiment. The direct-feedback configuration of the proposed architecture, illustrated in Fig. 2, is implemented and validated in experiments at sea with the DELFIMx ASC.

The INS is the backbone architecture that performs attitude, velocity and position numerical integration from rate gyro and accelerometer triads data, rigidly mounted on the vehicle structure (strapdown configuration) [3]. For highly maneuverable vehicles, the INS numerical integration must properly address the fast dynamics of inertial sensors output, to avoid estimation errors buildup. The INS computations adopted in this work account for high frequency attitude, velocity and position motions (denoted as coning, sculling, and scrolling, respectively), and are based on the algorithm developed in [3], [4]. The pure INS algorithm integrates the inertial sensor readings, and hence the results are corrupted by bias and noise, among other error

sources. The EKF is adopted to exploit aiding information and to dynamically compensate for the nonideal sensor characteristics that otherwise would yield unbounded inertial integration errors. Rate gyro and accelerometer biases compensation enhancements are obtained, using magnetometer measurements and selective frequency contents from gravity information, provided by the accelerometer triad readings.

A solution to integrate vector observations such as magnetometer and gravity measurements in the EKF is discussed. Although a snapshot attitude reconstruction can be obtained from the vector measurements using numerically efficient algorithms such as QUEST or TRIAD [5]–[7], the magnetometer and pendular readings are fed directly to the Kalman filter. The measurement residual is obtained by comparing the estimated and measured vector observations, and it is modeled in the filter as a function of the attitude estimation error. Consequently, the EKF acts as an attitude determination algorithm, by computing the perturbational attitude term based on vector observations. Vector measurement characteristics, such as sensor noise covariance, are described directly in the filter state model, yielding physical interpretation to the filter design parameters used in the computation of optimal gains.

The proposed vector aiding technique decomposes and optimally integrates gravitational observations in the EKF, taking into account the vehicle dynamics bandwidth information to properly trace inertial motion. Gravity readings are provided by the accelerometer triad, and hence distorted in the presence of linear and angular accelerations. A dynamic compensation of external accelerations is performed using the INS information to estimate angular acceleration, while linear acceleration is characterized in the frequency domain using the filter state space. Using this approach, the low frequency contents of the gravity readings are exploited by the EKF to compute the attitude estimation error. This paper develops and extends the work presented in [8] for the case of ASCs, deriving and tuning the proposed gravity reading integration to the specific dynamics of oceanic vehicles. Furthermore, experimental results obtained with the DELFIMx at sea validate the frequency domain mod-

eling technique, and illustrate its contribution to attitude and position estimation for the case of sparse/unavailable GPS signals.

Navigation system architectures for oceanic vehicles using Kalman filtering techniques are commonly adopted in the literature [9]–[15], and further references can be found in the valuable survey on ocean vehicle navigation [16]. The filter proposed in this work is based on the concept of multiplicative EKF (MEKF) [17], using the direction cosine matrix (DCM) form as the global attitude parametrization [18]. The linear differential equations of the filter are derived using a perturbational analysis of the vehicle kinematics, see [18] for an introduction on this framework. The adopted perturbational representation for the attitude error is locally linear and nonsingular, and consequently can be estimated by the Kalman filter, using the aiding measurements. The estimated attitude error is transferred from the EKF to the INS to update the nonlinear global attitude estimate, see Fig. 2, and reset in the filter. This incremental procedure can be regarded as a storage technique that prevents the filter’s attitude error estimates to fall outside the linearization region. As evidenced in [17], the uncertainty of the estimate, i.e., the estimation error covariance, is unaffected by the reset step. In this work, the attitude error is parameterized using the rotation vector representation in Earth coordinates. Other equivalent frame coordinates and attitude parametrization can be used, such as the Gibbs vector and modified Rodrigues parameters [17], [19].

The paper is organized as follows. Section II briefly discusses the INS integration algorithm adopted in this work. In Section III, the linear differential equations describing the inertial sensor errors are derived and introduced in the EKF state space model. In Section IV, the technique to use vector measurements directly in the EKF is derived and illustrated for magnetometer measurements. The method is extended for gravity measurements obtained from the accelerometer triad, which require modeling vehicle dynamics bandwidth information in the EKF to compensate for accelerated motion in the frequency domain. The EKF state space model is summarized in Section V, the discrete-time equivalent filter is obtained, and the correction and reset procedures to update the INS states using the EKF estimates are detailed. Simulation results to validate the proposed navigation system prior to experimental testing are shown in Section VI. Namely, the validity and influence of gravity selective frequency contents in the estimation results are studied. Experimental results obtained during the DELFIMx seatrials are presented in Section VII, to assess the navigation system performance in practice. Concluding remarks are found in Section VIII.

NOMENCLATURE

Column vectors and matrices are denoted respectively by lowercase and uppercase boldface type, e.g., \mathbf{s} and \mathbf{S} . The transpose of a vector or matrix will be indicated by a prime, and trailing subscripts $\{x, y, z\}$ denote the vector components, $\mathbf{s} = [s_x \ s_y \ s_z]'$. Leading subscripts and superscripts identify the coordinate system of a quantity, e.g., $^E\mathbf{s}$ is represented in coordinate frame $\{E\}$, and $^E_B\mathbf{R}$ is a rotation matrix that transforms the vector representation $^B\mathbf{s}$ into $^E\mathbf{s}$ by means of the linear operation $^E\mathbf{s} = ^E_B\mathbf{R}^B\mathbf{s}$. Position, velocity and acceleration are

denoted respectively by \mathbf{p} , \mathbf{v} , and \mathbf{a} , and the angular velocity of the vehicle expressed in body coordinates is represented by $\boldsymbol{\omega}$. The measurement and the estimate of quantity \mathbf{s} are denoted by \mathbf{s}_r and $\hat{\mathbf{s}}$, respectively. Discrete time quantities are characterized by the time index k subscript. The $(n \times n)$ identity matrix is denoted by \mathbf{I}_n , and $(m \times n)$ zeros and ones matrices are respectively denoted by $\mathbf{0}_{m \times n}$ and $\mathbf{1}_{m \times n}$, where the subscript is omitted whenever clear from the context.

II. INERTIAL NAVIGATION SYSTEM ALGORITHM

This section briefly introduces the high-accuracy inertial integration algorithm adopted in this work. Attitude and position integration is performed using the multirate computations derived in [3], [4], where a high-speed, low-order algorithm computes dynamic angular rate/acceleration effects at a small sampling interval, and its output is periodically fed to a moderate-speed algorithm that computes attitude/velocity resorting to exact, closed-form equations. Limited operational time and confined mission scenarios for the application at hand allowed for an invariant gravity model to be adopted without loss of precision, and the frame set is simplified to Earth and body frames, that are respectively denoted as $\{E\}$ and $\{B\}$, for a comprehensive description of reference frames the reader is referred to [18].

As depicted in Fig. 3, the inputs provided to the inertial algorithms are the inertial sensor output increments $\mathbf{v}(\tau) = \int_{t_{k-1}}^{\tau} \mathbf{a}_r dt$, $\boldsymbol{\alpha}(\tau) = \int_{t_{k-1}}^{\tau} \boldsymbol{\omega}_r dt$, which correspond to the integral of the strapdown accelerometer and rate gyro triads, corrupted by white noise and bias errors and modeled as follows:

$$\begin{aligned} \mathbf{a}_r &= {}^B\mathbf{a} - {}^B\mathbf{g} + \mathbf{b}_a + \mathbf{n}_a - \hat{\mathbf{b}}_a, \\ \boldsymbol{\omega}_r &= \boldsymbol{\omega} + \mathbf{b}_\omega + \mathbf{n}_\omega - \hat{\mathbf{b}}_\omega \end{aligned} \quad (1)$$

where \mathbf{g} represents Earth’s gravitational field, the sensor biases are denoted by \mathbf{b}_a and \mathbf{b}_ω , and $\mathbf{n}_a \sim \mathcal{N}(\mathbf{0}, \Xi_a)$, $\mathbf{n}_\omega \sim \mathcal{N}(\mathbf{0}, \Xi_\omega)$ are Gaussian white noises.

The attitude moderate-speed integration algorithm detailed in [3] computes body attitude in DCM form

$$\begin{aligned} &{}_{B_k}^{B_{k-1}}\mathbf{R}(\boldsymbol{\lambda}_k) \\ &= \mathbf{I}_3 + \frac{\sin(\|\boldsymbol{\lambda}_k\|)}{\|\boldsymbol{\lambda}_k\|}(\boldsymbol{\lambda}_k)_\times + \frac{1 - \cos(\|\boldsymbol{\lambda}_k\|)}{\|\boldsymbol{\lambda}_k\|^2}(\boldsymbol{\lambda}_k)_\times^2 \end{aligned} \quad (2)$$

where $\{B_k\}$ is the body frame at time k and $(\mathbf{s})_\times$ represents the skew symmetric matrix defined by the vector $\mathbf{s} \in \mathbb{R}^3$ such that $(\mathbf{s})_\times \mathbf{r} = \mathbf{s} \times \mathbf{r}$, $\mathbf{r} \in \mathbb{R}^3$. Rotation vector dynamics, based on Bortz’s equation [20], are formulated to denote angular integration and coning attitude terms $\boldsymbol{\alpha}_k$ and $\boldsymbol{\beta}_k$, respectively

$$\boldsymbol{\lambda}_k = \boldsymbol{\alpha}_k + \boldsymbol{\beta}_k \quad (3)$$

where $\boldsymbol{\alpha}_k = \boldsymbol{\alpha}(t)|_{t=t_k}$ and the coning attitude term measures the attitude changes due to the effects of angular rate vector rotation. A high-speed attitude algorithm is required to compute $\boldsymbol{\beta}_k$ as a summation of the high-frequency angular rate vector changes using simple, recursive computations [3]. Equations (2) and (3) summarize both the moderate and high-speed attitude dynamics

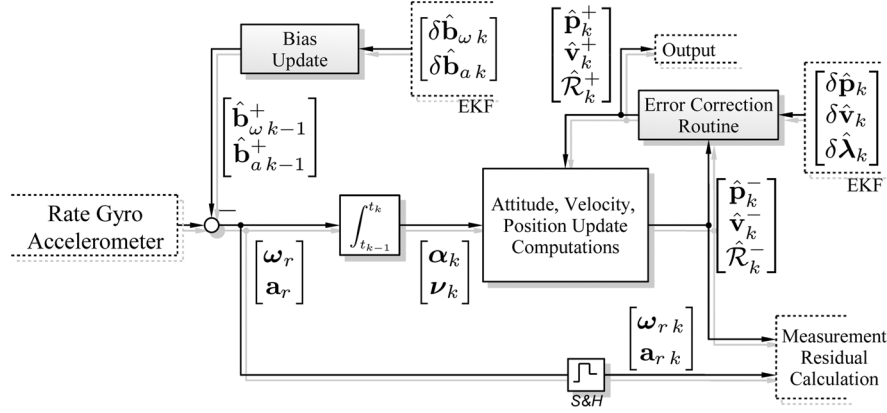


Fig. 3. Inertial navigation system with estimation error compensation. The inputs of the inertial integration algorithms are the attitude and velocity increments α_k and ν_k respectively, defined as the integration of the rate gyro and accelerometer readings over the sampling interval $[t_{k-1}, t_k]$. At each time step, the INS estimates $\hat{\mathbf{p}}_k^-$, $\hat{\mathbf{v}}_k^-$, and $\hat{\mathcal{R}}_k^-$ are provided to the EKF, and eventually corrected using the filter error estimates $\delta \hat{\mathbf{p}}_k$, $\delta \hat{\mathbf{v}}_k$, and $\delta \hat{\boldsymbol{\lambda}}_k$. The estimates of the sensor biases are dynamically updated using the filter estimates $\delta \hat{\mathbf{b}}_{\omega k}$ and $\delta \hat{\mathbf{b}}_{a k}$.

in the DCM format using exact, error-free equations, enabling high-accuracy results.

Exact linear velocity updates can be computed at moderate-speed rate using the equivalence between strapdown attitude and velocity/position algorithms [21], that yields

$$\mathbf{v}_k = \mathbf{v}_{k-1} + \frac{E}{B_{k-1}} \mathbf{R} \Delta^{B_{k-1}} \mathbf{v}_{SF k} + \Delta \mathbf{v}_{G/Cor k}$$

where $\Delta^{B_{k-1}} \mathbf{v}_{SF k}$ is the velocity increment related to the specific force, and $\Delta \mathbf{v}_{G/Cor k}$ represents the velocity increment due to gravity and Coriolis effects, see [4] for further details. The velocity increment $\Delta^{B_{k-1}} \mathbf{v}_{SF k}$ is described by high-speed components as follows:

$$\Delta^{B_{k-1}} \mathbf{v}_{SF k} = \mathbf{v}_k + \Delta \mathbf{v}_{rot k} + \Delta \mathbf{v}_{scul k}$$

where $\mathbf{v}_k = \mathbf{v}(t)|_{t=t_k}$, and $\Delta \mathbf{v}_{rot k}$ and $\Delta \mathbf{v}_{scul k}$ are the high-order velocity increments due to rotation and sculling, respectively, that are computed using high-frequency recursive equations [4].

Simulation environments and trajectory profiles to tune the algorithm's repetition rate according to the accuracy requirements are thoroughly described in [22] and algorithm evaluation procedures are presented in [3], [4]. Interestingly enough, high repetition rates can be implemented in a standard low-power consumption digital signal processing (DSP) based hardware architecture.

III. INERTIAL ERROR DYNAMICS

In a stand alone INS, bias and inertial sensor errors compensation is usually performed offline. The usage of filtering techniques in navigation systems, such as the EKF, allows for the dynamic estimation of inertial sensor nonidealities, bounding the INS errors. The EKF error equations adopted in this work are based on perturbational rigid body kinematics, and were brought to full detail in [18]. The nominal rigid body kinematics are given by

$$\begin{aligned} \dot{\mathbf{p}} &= \mathbf{v}, & \dot{\mathbf{v}} &= \mathcal{R}^B \mathbf{a}, & \dot{\mathcal{R}} &= \mathcal{R}(\boldsymbol{\omega})_{\times} \\ \dot{\mathbf{b}}_a &= \mathbf{n}_{b_a}, & \dot{\mathbf{b}}_{\omega} &= \mathbf{n}_{b_{\omega}} \end{aligned}$$

where \mathcal{R} is the shorthand notation for $\frac{E}{B} \mathbf{R}$, the inertial sensor biases are modeled as random walk processes, and $\mathbf{n}_{b_a} \sim \mathcal{N}(\mathbf{0}, \Xi_{b_a})$, $\mathbf{n}_{b_{\omega}} \sim \mathcal{N}(\mathbf{0}, \Xi_{b_{\omega}})$ are Gaussian white noises. The estimation errors are defined as

$$\begin{aligned} \delta \mathbf{p} &:= \hat{\mathbf{p}} - \mathbf{p}, & \delta \mathbf{v} &:= \hat{\mathbf{v}} - \mathbf{v}, & \delta \mathbf{b}_a &:= \hat{\mathbf{b}}_a - \mathbf{b}_a \\ \delta \mathbf{b}_{\omega} &:= \hat{\mathbf{b}}_{\omega} - \mathbf{b}_{\omega}, & (\delta \boldsymbol{\lambda})_{\times} &:= \hat{\mathcal{R}} \mathcal{R}' - \mathbf{I}_3 \end{aligned} \quad (4)$$

where the attitude error, denoted as $\delta \boldsymbol{\lambda}$, is parametrized by an unconstrained rotation vector representation in Earth coordinates, which can be assumed locally linear and nonsingular for "small-angle" attitude errors [18], for details and equivalent attitude parametrizations, see [17], [19].

The estimation error kinematics are obtained by retaining the first-order terms of Taylor's series expansions or by using perturbation algebraic techniques [18]. The continuous-time error state space model $\delta \dot{\mathbf{x}} = \mathbf{F}(\hat{\mathbf{x}}, \mathbf{u}) \delta \mathbf{x} + \mathbf{G}(\hat{\mathbf{x}}) \mathbf{n}_x$ is described by

$$\begin{aligned} \delta \mathbf{x} &= [\delta \mathbf{p}' \quad \delta \mathbf{v}' \quad \delta \boldsymbol{\lambda}' \quad \delta \mathbf{b}'_a \quad \delta \mathbf{b}'_{\omega}]' \\ \mathbf{n}_x &= [\mathbf{n}'_p \quad \mathbf{n}'_v \quad \mathbf{n}'_{\boldsymbol{\lambda}} \quad \mathbf{n}'_{b_a} \quad \mathbf{n}'_{b_{\omega}}]' \\ \mathbf{F}(\hat{\mathbf{x}}, \mathbf{u}) &= \begin{bmatrix} \mathbf{0} & \mathbf{I} & \mathbf{0} & \mathbf{0} & \mathbf{0} \\ \mathbf{0} & \mathbf{0} & -(\hat{\mathcal{R}} \mathbf{a}_r)_{\times} & -\hat{\mathcal{R}} & \mathbf{0} \\ \mathbf{0} & \mathbf{0} & \mathbf{0} & \mathbf{0} & -\hat{\mathcal{R}} \\ \mathbf{0} & \mathbf{0} & \mathbf{0} & \mathbf{0} & \mathbf{0} \\ \mathbf{0} & \mathbf{0} & \mathbf{0} & \mathbf{0} & \mathbf{0} \end{bmatrix} \\ \mathbf{G}(\hat{\mathbf{x}}) &= \text{blkdiag}(\mathbf{I}_3, \hat{\mathcal{R}}, \hat{\mathcal{R}}, -\mathbf{I}_3, -\mathbf{I}_3) \end{aligned} \quad (5)$$

where $\mathbf{x} = (\mathbf{p}, \mathbf{v}, \mathcal{R})$ are the quantities computed by the INS integration algorithm, $\mathbf{u} = (\mathbf{a}_r, \boldsymbol{\omega}_r)$ are the inertial measurements, $\text{blkdiag}(\cdot)$ denotes a block diagonal matrix defined by placing the matrix arguments along the main diagonal, $\mathbf{n}_v = \mathbf{n}_a$, and $\mathbf{n}_p \sim \mathcal{N}(\mathbf{0}, \Xi_p)$ is a Gaussian white noise that accounts for linearization and modeling errors and is used in the practical tuning of the filter, for more details the reader is referred to [8], [18].

After each filter update step, the EKF estimated inertial errors are transferred to the INS, as illustrated in Fig. 3. This technique preserves the small error assumption underlying the linearized model (5), combining local parametrization update in

the EKF with a global representation propagation and storage in the INS [17].

IV. VECTOR AIDING TECHNIQUES

The EKF relies on aiding sensor readings to successfully estimate the error states. The physical coupling between attitude and velocity errors expressed in (5) enables the use of GPS position readings to partially estimate attitude errors. As convincingly argued in [23], the observability of a GPS based navigation system with bias estimation can be analyzed using piece-wise time-invariant state models and, under that assumption, full observability is met by performing specific maneuvers along the desired trajectory. Recent work has been directed towards replacing the necessity for alignment maneuvers by equipping the filter with additional information sources, namely aiding sensors or vehicle dynamic model information, see [13], [24]–[26].

The vector observation technique enhances the system accuracy by providing attitude observations and vehicle dynamics bandwidth information to the EKF. For example, a self-contained TRIAD-like algorithm was previously adopted by the authors in [27], to compute an attitude matrix \mathcal{R}_{MPS} using the magnetometer triad readings and the Earth's gravitational field available from processing the accelerometer triad measurements. A straightforward but naive method to introduce the attitude measurement \mathcal{R}_{MPS} in the filter is obtained by defining the attitude measurement residual \mathbf{z}_{MPS} after the attitude error (4), yielding

$$(\mathbf{z}_{\text{MPS}})_\times = \hat{\mathcal{R}}\mathcal{R}'_{\text{MPS}} - \mathbf{I}_3$$

and modeling it in the filter as

$$\mathbf{z}_{\text{MPS}} = \delta\boldsymbol{\lambda} + \mathbf{n}_{\text{MPS}}$$

using a noise term \mathbf{n}_{MPS} to compensate for the effect of magnetometer, accelerometer, rate gyro and numerical disturbances on the attitude computation \mathcal{R}_{MPS} . Nonetheless, characterizing \mathbf{n}_{MPS} as white noise can degrade the filter performance because it does not properly model the nonlinear influence of pendular/magnetic sensors errors in \mathcal{R}_{MPS} computations. Also, the aiding attitude matrix \mathcal{R}_{MPS} is computed using the vector measurements available at each time instant (snapshot algorithm), and hence dynamic disturbances in the vector observation readings are not accounted for.

In this work, vector observations are embedded in the EKF, as depicted in Fig. 2. The magnetometer reading and gravity selective frequency contents provided by the accelerometer triad are modeled directly in the filter, bearing a more clear and accurate stochastic description of the measurement errors and disturbances.

The EKF implicitly computes the attitude based on the vector observations, presenting an alternate solution to Wahba's problem [5], [28] that encloses system dynamics, without external attitude determination algorithms and using optimality criteria. Sensor error characteristics other than just white noise are properly modeled in the filter, using the EKF covariance matrices and the structure of the error state space model. The algorithm presented herein can be generalized to any number of vector observations, devising a straightforward procedure to

enhance the accuracy of the navigation system results, which also reinforces the EKF linearization assumption.

A. Vector Measurement Residual Model

The attitude measurement residual is obtained by comparing the estimated and the measured vectors. The considered vector measurement model is

$$\mathbf{s}_r = \mathcal{R}'^E \mathbf{s} + \mathbf{n}_s \quad (6)$$

where $\mathbf{n}_s \sim \mathcal{N}(\mathbf{0}, \Xi_s)$ is a Gaussian white noise. The attitude measurement residual in Earth frame coordinates is described by

$${}^E \mathbf{z}_s = {}^E \mathbf{s} - \hat{\mathcal{R}} \mathbf{s}_r.$$

Using the sensor model (6) and replacing the INS attitude estimate $\hat{\mathcal{R}}$ by the attitude error approximation $\hat{\mathcal{R}} \approx (\mathbf{I}_3 + (\delta\boldsymbol{\lambda})_\times) \mathcal{R}$ yields

$${}^E \mathbf{z}_s = {}^E \mathbf{s} - \hat{\mathcal{R}} \mathcal{R}'^E \mathbf{s} - \hat{\mathcal{R}} \mathbf{n}_s \approx -(\delta\boldsymbol{\lambda})_\times {}^E \mathbf{s} - \hat{\mathcal{R}} \mathbf{n}_s$$

which relates the EKF measurement residual ${}^E \mathbf{z}_s$ with the attitude error $\delta\boldsymbol{\lambda}$, producing the linearized model

$${}^E \mathbf{z}_s = ({}^E \mathbf{s})_\times \delta\boldsymbol{\lambda} - \hat{\mathcal{R}} \mathbf{n}_s. \quad (7)$$

The measurement residual can be represented in Earth or in body frame coordinates, which are related by a rotation transformation and hence contains the same information. Repeating the same algebraic manipulations, the linearized model of the measurement residual in body coordinates is given by

$${}^B \mathbf{z}_s := \hat{\mathcal{R}}' {}^E \mathbf{s} - \mathbf{s}_r \approx \hat{\mathcal{R}}' ({}^E \mathbf{s})_\times \delta\boldsymbol{\lambda} - \mathbf{n}_s. \quad (8)$$

Although the measurement residuals (7) and (8) describe the same attitude information, the linearized measurement matrix for (7) is constant and the components of $\delta\boldsymbol{\lambda}$ can be related directly with those of ${}^E \mathbf{z}_s$. For example, the measurement model (7) for the vector ${}^E \mathbf{s} = [0 \ 0 \ 1]'$ is given by ${}^E \mathbf{z}_s = [-\delta\lambda_y \ \delta\lambda_x \ 0]'$ – $\hat{\mathcal{R}} \mathbf{n}_s$, that contains information solely about the rotation error along the x-axis and y-axis, and illustrates the fact that the yaw angle error, i.e., $\delta\lambda_z$, cannot be determined by gravity readings.

In general, the vector reading \mathbf{s}_r can be corrupted by other additive sensor disturbances, namely biases \mathbf{b}_s , and dynamic disturbances \mathbf{d}_s , as follows:

$$\mathbf{s}_r = \mathcal{R}'^E \mathbf{s} + \mathbf{n}_s - \delta\mathbf{b}_s + \mathbf{d}_s \quad (9)$$

where $\delta\mathbf{b}_s$ is the bias compensation error term, and \mathbf{d}_s is the output of a process modeled in the state space form. The linearized measurement residual representations for the sensor reading (9), in Earth and in body coordinates, are respectively described by

$$\begin{aligned} {}^E \mathbf{z}_s &= ({}^E \mathbf{s})_\times \delta\boldsymbol{\lambda} + \hat{\mathcal{R}} \delta\mathbf{b}_s - \hat{\mathcal{R}} \mathbf{d}_s - \hat{\mathcal{R}} \mathbf{n}_s \\ {}^B \mathbf{z}_s &= \hat{\mathcal{R}}' ({}^E \mathbf{s})_\times \delta\boldsymbol{\lambda} + \delta\mathbf{b}_s - \mathbf{d}_s - \mathbf{n}_s. \end{aligned} \quad (10)$$

Using the measurement model (10), vector observations obtained by sensors such as pendulums and magnetometers can be introduced directly in the EKF. The sensor nonidealities are

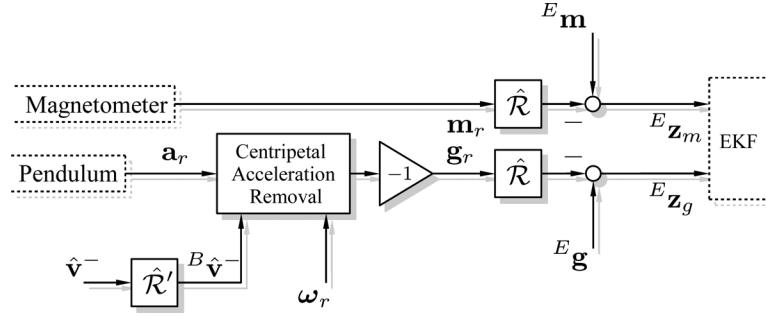


Fig. 4. Vector measurement residual computation (magnetometer and gravity). The measurement residuals are obtained by comparing the measured and the expected vectors. The influence of angular accelerations in the pendular reading \mathbf{g}_r is compensated using the linear and angular velocities provided by the INS; the influence of linear accelerations is compensated dynamically in the EKF state space.

modeled in the filter, as opposed to using intermediate attitude reconstruction, which allows for the integration of any number of vector measurements, at different sampling rates, and compensating for dynamic disturbances. The observation noise covariance matrix, used in the computation of the optimal feedback gains, is directly given by the sensor noise variance Ξ_s .

B. Magnetic and Pendular Measurements Integration

The magnetometer model considered in this work is given by

$$\mathbf{m}_r = \mathcal{R}'^E \mathbf{m} + \mathbf{n}_m \quad (11)$$

where \mathbf{m} denotes Earth's magnetic field, $\mathbf{n}_m \sim \mathcal{N}(\mathbf{0}, \Xi_m)$ is a Gaussian white noise, and magnetic distortions such as soft iron and hard iron are compensated offline using calibration algorithms available in the literature [29], [30]. The sensor description (11) is identical to the vector reading description (6). As illustrated in Fig. 4, the measurement residual (7) is adopted to integrate the magnetometer information in the EKF, yielding

$$\mathbf{z}_m := {}^E \mathbf{m} - \hat{\mathcal{R}} \mathbf{m}_r = ({}^E \mathbf{m})_{\times} \delta \boldsymbol{\lambda} - \hat{\mathcal{R}} \mathbf{n}_m.$$

A gravity vector measurement is obtained from the accelerometer reading (1), which can be decomposed in Coriolis and linear acceleration components

$$\mathbf{a}_r = \frac{d^B \mathbf{v}}{dt} + \boldsymbol{\omega} \times {}^B \mathbf{v} - {}^B \mathbf{g} - \delta \mathbf{b}_a + \mathbf{n}_a. \quad (12)$$

To obtain a gravity measurement reading \mathbf{g}_r , adequate modeling is adopted to remove the acceleration terms in (12). Typical maneuvers of autonomous oceanic vehicles involve mostly short term linear accelerations, and hence the $(d^B \mathbf{v})/(dt)$ term is modeled in the filter state model as a high-frequency process. The Coriolis term $\boldsymbol{\omega} \times {}^B \mathbf{v}$ occurs in transient but also in trimming maneuvers such as helicoidal paths, and is compensated for using the linear and angular velocities information provided by the INS. The gravity vector measurement \mathbf{g}_r is given by

$$\begin{aligned} \mathbf{g}_r &\triangleq -(\mathbf{a}_r - \hat{\boldsymbol{\omega}} \times {}^B \hat{\mathbf{v}}) \\ &= {}^B \mathbf{g} - \frac{d^B \mathbf{v}}{dt} + \delta(\boldsymbol{\omega} \times {}^B \mathbf{v}) + \delta \mathbf{b}_a - \mathbf{n}_a. \end{aligned} \quad (13)$$

where the $\delta(\boldsymbol{\omega} \times {}^B \mathbf{v}) = \hat{\boldsymbol{\omega}} \times {}^B \hat{\mathbf{v}} - \boldsymbol{\omega} \times {}^B \mathbf{v}$ is the error of the centripetal acceleration removal, and ${}^B \hat{\mathbf{v}} = \hat{\mathcal{R}}' {}^E \mathbf{v}$ is the

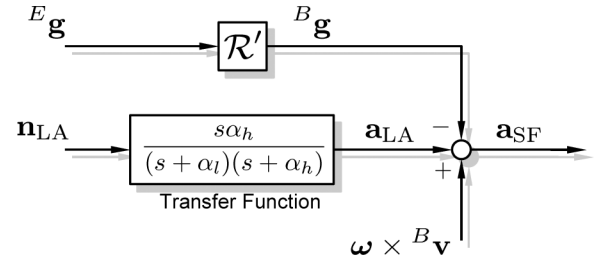


Fig. 5. Pendular measurement model: the accelerometer measurement is characterized in the filter as the sum of gravitational, angular, and linear accelerations, where the latter is modeled as a bandpass process in the filter state space.

estimated velocity in body coordinates. The gravity reading (13) is modeled as

$$\mathbf{g}_r = {}^B \mathbf{g} - \mathbf{a}_{LA} + \delta(\boldsymbol{\omega} \times {}^B \mathbf{v}) + \delta \mathbf{b}_a - \mathbf{n}_a \quad (14)$$

where $\mathbf{a}_{LA} = [a_{LAx} \ a_{LAy} \ a_{LAz}]'$ represents the linear acceleration estimate. Each of the \mathbf{a}_{LA} components is modeled as a bandpass signal whose bandwidth is shaped according to the vehicle characteristics, often to filter out high-frequency accelerometer jitter and to simultaneously avoid the influence of erroneous low-frequency accelerometer bias. The state model dynamics for the x-axis component, is generically represented in Fig. 5, and can be written as

$$\begin{aligned} \dot{\mathbf{x}}_{LAx} &= \begin{bmatrix} 0 & 1 \\ -\alpha_h \alpha_l & -(\alpha_h + \alpha_l) \end{bmatrix} \mathbf{x}_{LAx} + \begin{bmatrix} 0 \\ \alpha_h \end{bmatrix} n_{LAx} \\ a_{LAx} &= [0, \ 1] \mathbf{x}_{LAx}. \end{aligned} \quad (15)$$

where α_h and α_l are the high-frequency and low-frequency cutoff frequencies, respectively, and n_{LAx} is modeled as a zero-mean, Gaussian white noise process with variance σ_{LA}^2 .

Using the results for the vector reading model (9), the measurement residual for the gravity reading (13) is defined as ${}^E \mathbf{z}_g = {}^E \mathbf{g} - \hat{\mathcal{R}} \mathbf{g}_r$ and the first-order formulation is given by

$${}^E \mathbf{z}_g \approx ({}^E \mathbf{g})_{\times} \delta \boldsymbol{\lambda} - \hat{\mathcal{R}} \delta \mathbf{b}_a - \hat{\mathcal{R}} \delta(\boldsymbol{\omega} \times {}^B \mathbf{v}) + \hat{\mathcal{R}} \mathbf{a}_{LA} + \hat{\mathcal{R}} \mathbf{n}_a.$$

Using (1) and (4), the centripetal acceleration compensation term is given by

$$\begin{aligned} \delta(\boldsymbol{\omega} \times {}^B \mathbf{v}) &\approx (\hat{\boldsymbol{\omega}})_{\times} \hat{\mathcal{R}}' \delta \mathbf{v} + (\hat{\boldsymbol{\omega}})_{\times} ({}^B \hat{\mathbf{v}})_{\times} \hat{\mathcal{R}}' \delta \boldsymbol{\lambda} + ({}^B \hat{\mathbf{v}})_{\times} (\delta \mathbf{b}_\omega - \mathbf{n}_\omega) \end{aligned}$$

and the observation equation of the gravity measurement residual is

$$\begin{aligned} {}^E\mathbf{z}_g = & -(\hat{\mathbf{R}}\hat{\boldsymbol{\omega}})_{\times}\delta\mathbf{v} + \left(({}^E\mathbf{g})_{\times} - (\hat{\mathbf{R}}\hat{\boldsymbol{\omega}})_{\times}({}^E\hat{\mathbf{v}})_{\times} \right)\delta\boldsymbol{\lambda} \\ & -\hat{\mathbf{R}}\delta\mathbf{b}_a - ({}^E\hat{\mathbf{v}})_{\times}\hat{\mathbf{R}}\delta\mathbf{b}_w + \hat{\mathbf{R}}\mathbf{a}_{\text{LA}} + \hat{\mathbf{R}}\mathbf{n}_a + ({}^E\hat{\mathbf{v}})_{\times}\hat{\mathbf{R}}\mathbf{n}_w \end{aligned} \quad (16)$$

where \mathbf{a}_{LA} is the output of triaxial generalization of the state model dynamics (15), integrated in the EKF, and tuned according to the maneuverability characteristics of the vehicles.

Fig. 4 illustrates the computation of the gravity measurement residual ${}^E\mathbf{z}_g$, which is fed to the filter using the observation model (16). While the INS calculates the body attitude estimates using high-precision algorithms described in Section II, the EKF estimates the attitude, velocity, position errors using the aiding sensor measurements. The INS estimates are corrected using the errors estimated by the EKF, which are then reset without influencing the estimation error covariance [17], thus keeping the first-order approximation of the filter model valid.

V. IMPLEMENTATION

The continuous-time state space model $\dot{\mathbf{x}}_C = \mathbf{F}_C(\hat{\mathbf{x}}, \mathbf{u})\mathbf{x}_C + \mathbf{G}_C(\hat{\mathbf{x}})\mathbf{n}_{x_C}$ adopted in the filter is described by

$$\begin{aligned} \mathbf{x}_C &= [\delta\mathbf{x}' \quad \mathbf{x}'_{\text{LA}x} \quad \mathbf{x}'_{\text{LA}y} \quad \mathbf{x}'_{\text{LA}z}]', \\ \mathbf{n}_{x_C} &= [\mathbf{n}'_x \quad n_{\text{LA}x} \quad n_{\text{LA}y} \quad n_{\text{LA}z}]', \\ \mathbf{F}_C(\mathbf{x}, \mathbf{u}) &= \text{blkdiag}(\mathbf{F}(\mathbf{x}, \mathbf{u}), \mathbf{F}_{\text{LA}}, \mathbf{F}_{\text{LA}}, \mathbf{F}_{\text{LA}}) \\ \mathbf{G}_C(\mathbf{x}) &= \text{blkdiag}(\mathbf{G}(\mathbf{x}), \mathbf{G}_{\text{LA}}, \mathbf{G}_{\text{LA}}, \mathbf{G}_{\text{LA}}) \\ \mathbf{F}_{\text{LA}} &= \begin{bmatrix} 0, & 1 \\ -\alpha_l\alpha_h, & -(\alpha_l + \alpha_h) \end{bmatrix} \\ \mathbf{G}_{\text{LA}} &= \begin{bmatrix} 0 \\ \alpha_h \end{bmatrix} \end{aligned}$$

where $\delta\mathbf{x}$, \mathbf{n}_x , $\mathbf{F}(\mathbf{x}, \mathbf{u})$ and $\mathbf{G}(\mathbf{x})$ are defined in (5). The measurement model $\mathbf{z} = \mathbf{H}(\hat{\mathbf{x}}, \mathbf{u})\mathbf{x}_C + \mathbf{n}_z$ can be written as (17) shown at the bottom of the page where \mathbf{n}_g is a fictitious white noise associated with \mathbf{z}_g observation, and \mathbf{z}_{GPS} is the GPS measurement residual, classically defined by the difference between the position estimated by the INS and that measured by the GPS [31], that is

$$\mathbf{z}_{\text{GPS}} := \hat{\mathbf{p}} - \mathbf{p}_{\text{GPS}} = \delta\mathbf{p} - \mathbf{n}_{\text{GPS}},$$

where $\mathbf{n}_{\text{GPS}} \sim \mathcal{N}(\mathbf{0}, \Xi_{\text{GPS}})$ is a Gaussian white noise that models the GPS measurement noise.

The state and observation noise covariance matrices are

$$\begin{aligned} \mathbf{Q}_C &= \text{blkdiag}(\Xi_p, \Xi_a, \Xi_\omega, \Xi_{b_a}, \Xi_{b_w}, \Xi_{\text{LA}}), \\ \mathbf{R}_C(\hat{\mathbf{x}}) &= \text{blkdiag}(\Xi_{\text{GPS}}, \Xi_m, \hat{\mathbf{R}}\Xi_a\hat{\mathbf{R}}' \\ &\quad - ({}^E\hat{\mathbf{v}})_{\times}\hat{\mathbf{R}}\Xi_\omega\hat{\mathbf{R}}'({}^E\hat{\mathbf{v}})_{\times} + \hat{\mathbf{R}}\Xi_g\hat{\mathbf{R}}') \end{aligned}$$

where $\Xi_{\text{LA}} = \sigma_{\text{LA}}^2 \mathbf{I}_3$. The discrete-time state space model

$$\mathbf{x}_{k+1} = \Phi_k\mathbf{x}_k + \mathbf{w}_k, \quad \mathbf{z}_k = \mathbf{H}_k\mathbf{x}_k + \mathbf{v}_k$$

is obtained by sample-and-hold of the inputs [31], and hence $\Phi_k = e^{\mathbf{F}_k T}$, $\mathbf{H}_k = \mathbf{H}(\mathbf{x}, \mathbf{u})|_{t=t_k}$, and the discrete-time noise covariance matrices are [32] $\mathbf{Q}_k \simeq \mathbf{G}_k\mathbf{Q}_C\mathbf{G}_k'T$, $\mathbf{R}_k \simeq (\mathbf{R}_{Ck})/(T)$, where T is the sampling period, $\mathbf{F}_k = \mathbf{F}_C(\mathbf{x}, \mathbf{u})|_{t=t_k}$, $\mathbf{G}_k = \mathbf{G}_C(\mathbf{x})|_{t=t_k}$, $\mathbf{R}_{Ck} = \mathbf{R}_C(\mathbf{x})|_{t=t_k}$ and $\Phi_k = \Phi(t_{k+1}, t_k)$ denotes the state transition matrix.

The gravity measurement residual ${}^E\mathbf{z}_g$ introduces state and measurement noise correlation matrix [31]

$$\begin{aligned} \mathbf{C}_C(\hat{\mathbf{x}}) &= \begin{bmatrix} \mathbf{0} & \mathbf{0} & \mathbf{0} & \mathbf{0} & \mathbf{0} & \mathbf{0} \\ \mathbf{0} & \mathbf{0} & \mathbf{0} & \mathbf{0} & \mathbf{0} & \mathbf{0} \\ \mathbf{0} & -\hat{\mathbf{R}}\Xi_a & -({}^E\hat{\mathbf{v}})'_{\times}\hat{\mathbf{R}}\Xi_\omega & \mathbf{0} & \mathbf{0} & \mathbf{0} \end{bmatrix}', \\ \mathbf{C}_k &= \frac{1}{T} \int_{t_{k-1}}^{t_k} \phi(t_k, \tau)\mathbf{G}(\tau)\mathbf{C}_C(\tau)d\tau \\ &\simeq \left(\mathbf{I}_3 + \frac{\mathbf{F}_k T}{2} \right) \mathbf{G}_k\mathbf{C}_C \end{aligned}$$

where $\mathbf{C}_C(\mathbf{x})$ is the continuous state and measurement noises correlation matrix and $\mathbf{C}_{Ck} = \mathbf{C}_C(\mathbf{x})|_{t=t_k}$. The discrete-time equivalent matrix \mathbf{C}_k is computed using a first-order approximation similar to those discussed in [31] for \mathbf{Q}_k and \mathbf{R}_k . The following Kalman gains and error covariance matrix equations are modified to include the state and measurement noises correlation matrix:

$$\begin{aligned} \mathbf{K}_k &= (\mathbf{P}_k^- \mathbf{H}_k' + \mathbf{C}_k)[\mathbf{H}_k\mathbf{P}_k^- \mathbf{H}_k' + \mathbf{R}_k + \mathbf{H}_k\mathbf{C}_k \\ &\quad + \mathbf{C}_k' \mathbf{H}_k']^{-1}, \\ \mathbf{P}_k^+ &= (\mathbf{I}_n - \mathbf{K}_k\mathbf{H}_k)\mathbf{P}_k^- - \mathbf{K}_k\mathbf{C}_k' \end{aligned}$$

and the filter covariance matrix is updated using $\mathbf{P}_{k+1}^- = \Phi_k\mathbf{P}_k^+\Phi_k' + \mathbf{Q}_k$.

After each EKF update, error estimates are fed into the INS error correction routines as depicted in Figs. 2 and 3, where the quantities predicted by the INS are denoted by the superscript $-$ and the updated quantities are identified with the superscript $+$. It is important to stress that linearization assumptions are kept valid during the algorithm execution since the EKF error

$$\begin{aligned} \mathbf{z} &= [\mathbf{z}'_{\text{GPS}} \quad {}^E\mathbf{z}'_m \quad {}^E\mathbf{z}'_g] \\ \mathbf{n}_z &= [-\mathbf{n}'_{\text{GPS}} \quad -\hat{\mathbf{R}}\mathbf{n}'_m \quad (-\hat{\mathbf{R}}\mathbf{n}_a + ({}^E\hat{\mathbf{v}})_{\times}\hat{\mathbf{R}}\mathbf{n}_w + \hat{\mathbf{R}}\mathbf{n}_g)'] \\ \mathbf{H}(\hat{\mathbf{x}}, \mathbf{u}) &= \begin{bmatrix} \mathbf{I}_3 & \mathbf{0} & \mathbf{0} & \mathbf{0} & \mathbf{0} & \mathbf{0} \\ \mathbf{0} & \mathbf{0} & ({}^E\mathbf{m})_{\times} & \mathbf{0} & \mathbf{0} & \mathbf{0} \\ \mathbf{0} & (\hat{\mathbf{R}}\boldsymbol{\omega})_{\times} & ({}^E\mathbf{g})_{\times} + (\hat{\mathbf{R}}\boldsymbol{\omega})_{\times}({}^E\hat{\mathbf{v}})_{\times} & -\hat{\mathbf{R}} & -({}^E\hat{\mathbf{v}})_{\times}\hat{\mathbf{R}} & \hat{\mathbf{R}}\mathbf{H}_{\text{LA}} \end{bmatrix} \\ \mathbf{H}_{\text{LA}} &= \text{blkdiag}([0 \quad -1], [0 \quad -1], [0 \quad -1]) \end{aligned} \quad (17)$$

estimates are reset after being used to compensate the corresponding variables. The error correction procedures are specific to the inertial integration algorithms and error state space representations. For the inertial integration algorithms described in Section II, error routines are detailed next.

The attitude estimate is compensated using

$$\hat{\mathcal{R}}_k^+ = \mathbf{R}'(\delta\hat{\boldsymbol{\lambda}}_k)\hat{\mathcal{R}}_k^- \quad (18)$$

where $\mathbf{R}'(\delta\hat{\boldsymbol{\lambda}}_k) = \mathbf{I}_3 - (\sin(\|\delta\hat{\boldsymbol{\lambda}}_k\|))/(\|\delta\hat{\boldsymbol{\lambda}}_k\|)(\delta\hat{\boldsymbol{\lambda}}_k)_\times + (1 - \cos(\|\delta\hat{\boldsymbol{\lambda}}_k\|))/(\|\delta\hat{\boldsymbol{\lambda}}_k\|^2)(\delta\hat{\boldsymbol{\lambda}}_k)_\times^2$ is computationally implemented using power series expansion of the scalar trigonometric terms up to an arbitrary accuracy [22]. The remaining state variables are simply compensated using

$$\begin{aligned} \hat{\mathbf{p}}_k^+ &= \hat{\mathbf{p}}_k^- - \delta\hat{\mathbf{p}}_k, & \hat{\mathbf{v}}_k^+ &= \hat{\mathbf{v}}_k^- - \delta\hat{\mathbf{v}}_k \\ \hat{\mathbf{b}}_{a_k}^+ &= \hat{\mathbf{b}}_{a_k}^- - \delta\hat{\mathbf{b}}_{a_k}, & \hat{\mathbf{b}}_{\omega_k}^+ &= \hat{\mathbf{b}}_{\omega_k}^- - \delta\hat{\mathbf{b}}_{\omega_k}. \end{aligned} \quad (19)$$

The block structure of the INS with EKF corrections is depicted in Fig. 3, where the error compensation and bias update routines, (18) and (19) respectively, are executed after the INS outputs have been fed to the EKF and errors estimates are available. Note that the EKF sampling rate is synchronized with the moderate-speed INS output rate and that no corrections are involved in the high-speed computation algorithms. After the error correction procedure is completed, the EKF error estimates are reset $\delta\hat{\mathbf{x}}_k = 0$. The INS error correction and EKF estimate reset do not influence the uncertainty of the estimated quantities, and hence the estimation error covariance is unaffected by this procedure [17]. At the start of the next computation cycle ($t = t_{k+1}$), the INS attitude and velocity/position updates presented in Section II are performed on the corrected estimates ($\hat{\mathcal{R}}_k^+, \hat{\mathbf{v}}_k^+, \hat{\mathbf{p}}_k^+$) to provide new inputs ($\hat{\mathcal{R}}_{k+1}^-, \hat{\mathbf{v}}_{k+1}^-, \hat{\mathbf{p}}_{k+1}^-$) to the EKF.

VI. SIMULATION RESULTS

This section presents a simulation study of the proposed navigation system, prior to the practical implementation of the algorithm in the autonomous surface craft. The impact of the vector observation in the estimation results is analyzed, by considering three case study simulations. In the first case, the navigation system is initialized with large estimation errors to show how the estimation results can be enhanced by the use of the proposed frequency domain sensor integration technique. In this test, the vehicle describes a standard rigid body trimming trajectory with constant centripetal acceleration to demonstrate the necessity of centripetal acceleration removal in the pendular measurements. The linear acceleration model (14) is validated in the second case study, by presenting the response of the navigation system when the vehicle is subject to a step acceleration with damping. In the last case study, poor GPS signal detection is simulated to illustrate how the position estimates remain within acceptable bounds by means of the pendular measurements.

The INS high-speed algorithm is executed at 100 Hz and the normal-speed algorithm is synchronized with the EKF discrete time frequency of 50 Hz. The GPS position measurements are obtained at the nominal frequency of 1 Hz. The characteristics of the simulated inertial and aiding sensors are presented in Table I.

TABLE I
SENSOR NONIDEALITIES

Sensor	Bias	Noise Variance
Rate Gyro	5 °/s	(0.02 °/s) ²
Accelerometer	0.12 m/s ²	(0.006 m/s ²) ²
Magnetometer (calibrated)	-	(60 μG) ²
GPS	-	10 m ²

A. Initial Calibration Error

The contribution of the magnetic and pendular measurements to the accuracy of the estimates is studied for the initial estimation error of 5° in the roll angle, and calibration errors in the rate gyro and accelerometer bias given by $\delta b_{\omega_x} = 0.57^\circ/\text{s}$ and $\delta b_{a_z} = 0.01 \text{ m/s}^2$, respectively. The rigid body describes the ascending helix depicted in Fig. 6(a), which is a standard trimming trajectory subject to constant centripetal acceleration. The convergence of the estimation errors in Fig. 6(b), (c), and (d) shows that the pendular readings enhance the observability of errors such as the gyro bias, roll angle and vertical accelerometer bias, as expected from physical intuition and analysis of the observability matrix for trimming trajectories. Interestingly enough, the obtained estimation results were stable and accurate although the small error assumption underlying the EKF derivation was not verified by the initial estimation errors.

B. Linear Accelerated Motion

The impact of the vector aiding in the navigation system results is analyzed for the case of a straight line trajectory. The vehicle is subject to a constant acceleration input that is progressively compensated by the linear drag effects, as depicted in Fig. 7(a), and linear uniform motion is attained. Fig. 7(b) validates the assumption that the vehicle's linear acceleration component in \mathbf{z}_g can be modeled as a bandpass signal (15), and hence the low frequency contents of \mathbf{z}_g are used to estimate the inertial system errors. Numerical results obtained with the proposed technique are presented in Table II, where improvements due to the inclusion of aiding vector observations are evidenced.

C. Trimming Trajectory

The medium term navigation system behavior is assessed for the trimming trajectory with standard initial estimation errors. Fig. 8 demonstrates the performance enhancements introduced by the magnetometer readings and the selective frequency contents of the accelerometers measurements. As presented in Table III, the magnetometer readings smooth out yaw errors, and pendular observations enhance the estimation of roll and pitch. Also, the constant centripetal acceleration of the trimming trajectory is successfully compensated for. The x- and y-axes position errors are improved by the magnetic and pendular observations, respectively, as expected from the velocity and attitude errors correlation term $(\hat{\mathcal{R}}\mathbf{a}_r)_\times$ expressed in (5). The measured acceleration is dominated by the gravitational acceleration and hence

$$(\hat{\mathcal{R}}\mathbf{a}_r)_\times \approx \begin{bmatrix} 0 & g & E_{a_y} \\ -g & 0 & -E_{a_x} \\ -E_{a_y} & E_{a_x} & 0 \end{bmatrix}$$

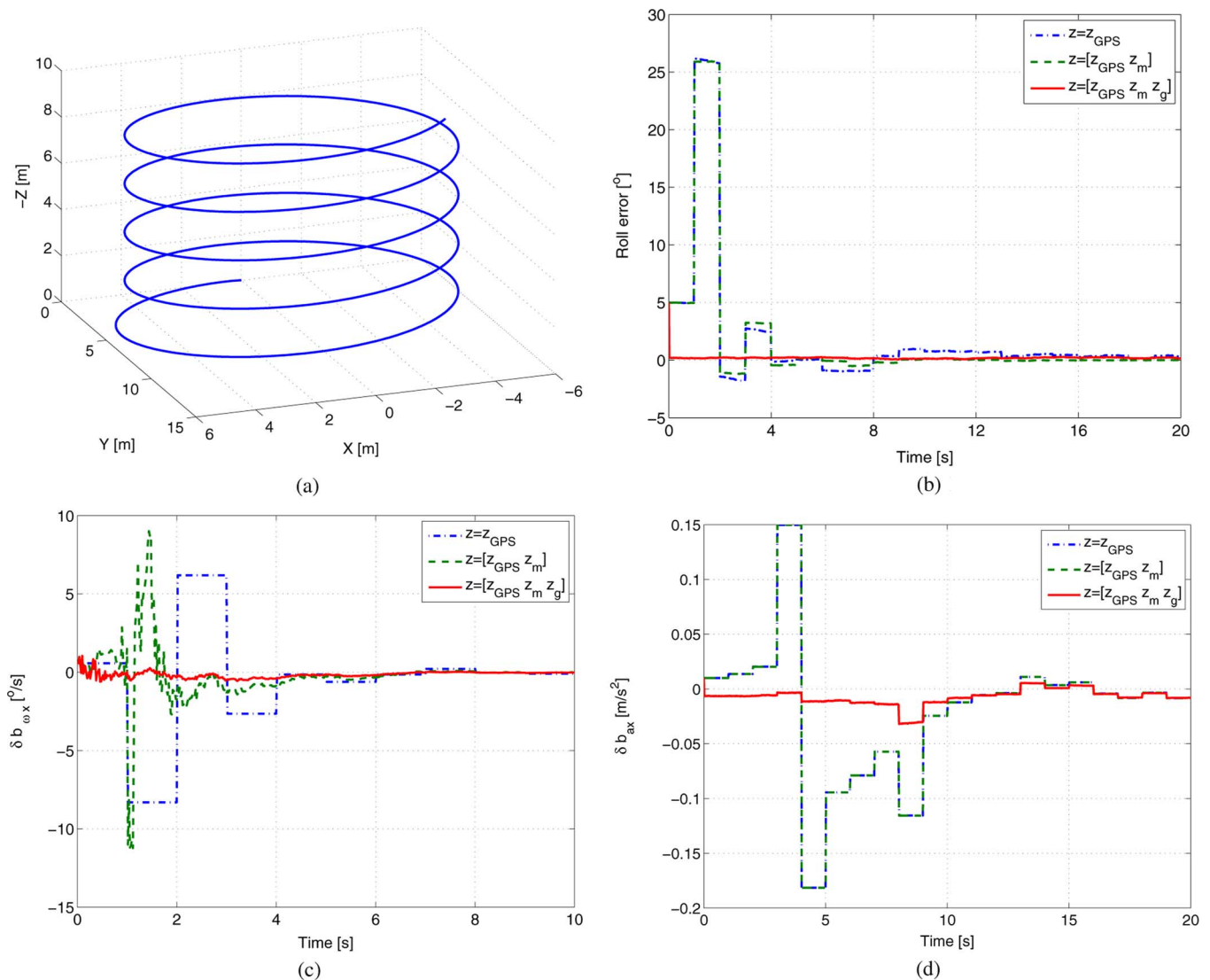


Fig. 6. Initial estimation error compensation: for a trimming trajectory subject to constant centripetal acceleration, the simulation results show that estimation errors are clearly enhanced by the pendular readings contained in \mathbf{z}_g . (a) Trimming trajectory. (b) Roll estimation error. (c) X-axis rate gyro bias estimation error. (d) Z-axis accelerometer bias estimation error.

where E_{a_x} and E_{a_y} are determined by the centripetal acceleration. As suggested by Fig. 7(b), the steady-state magnitude of the centripetal acceleration is small with respect to g and hence improvements in the z-axis position estimate are negligible for the considered trimming trajectory.

Simulation results for a GPS signal with output frequency of 0.2 Hz are depicted in Fig. 9, with and without pendular measurement aiding. The figure shows that x- and y-axes position estimates are enhanced by the selective frequency contents of the accelerometers measurements. The filter exploits the pendular measurements, limiting the position estimate divergence when the GPS signal is sparse, and extending the navigation system autonomy with respect to the GPS aiding source.

VII. EXPERIMENTAL RESULTS

The proposed navigation system is validated using a low-power hardware architecture enclosing low-cost sensors and mounted on-board the DELFIMx catamaran. This section

details the characteristics of the DELFIMx oceanic vessel and introduces the hardware architecture adopted to collect and process experimental data. Experimental results obtained at sea illustrate the performance of the navigation system in practice for standard ASC trajectories, emphasizing its robustness characteristics. Namely, the compensation of the pendular measurements disturbances in the frequency domain is validated, and the autonomy of the navigation system with respect to GPS measurements is demonstrated.

A. DELFIMx ASC and Sensor Characteristics

The DELFIMx craft, depicted in Fig. 1, was adopted in the experimental validation of the proposed navigation system. For integrated guidance and control, a path-following control strategy was adopted due to its enhanced performance, which translates into smoother convergence to the path and less demand on the control effort [33]. The vehicle has a wing-shaped, central structure that is lowered during operations at sea. At the bottom of this structure, a low-drag body

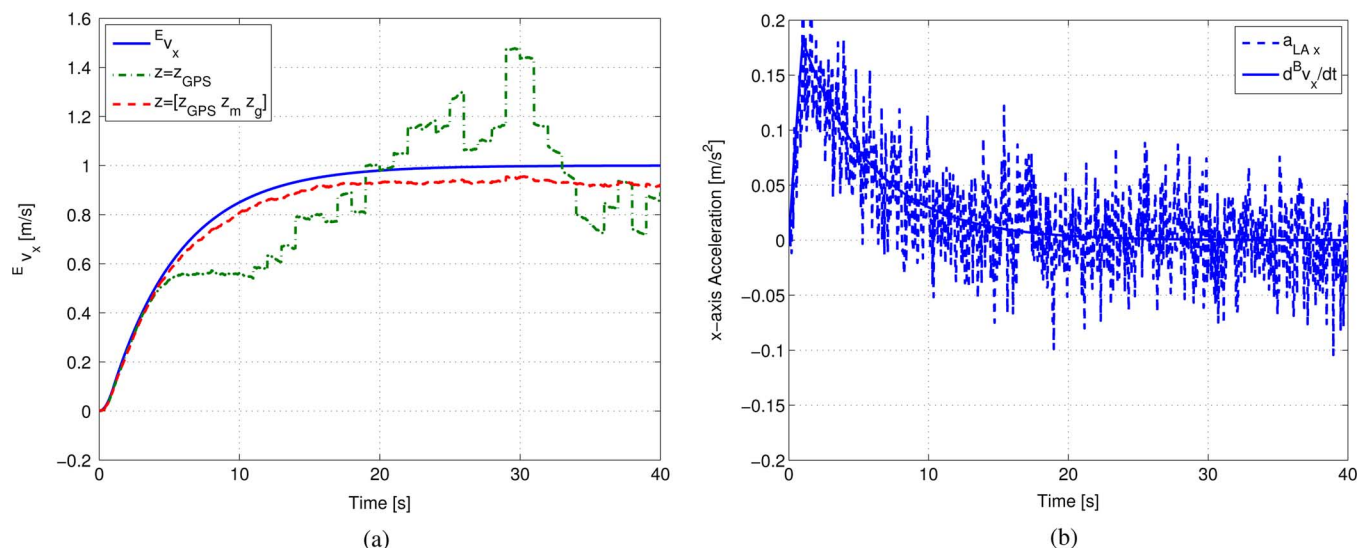


Fig. 7. Linear accelerated motion compensation results: (a) the pendular reading enhances velocity estimation, in spite of the linear acceleration perturbation contained in z_g , (b) the linear acceleration is properly tracked by the filter using the bandpass model. (a) Velocity profile. (b) Linear acceleration estimation.

TABLE II
FILTER RESULTS, STRAIGHT PATH TRAJECTORY

	Root Mean Square (RMS) Error					
	p_x (m)	p_y (m)	p_z (m)	Yaw ($^\circ$)	Pitch ($^\circ$)	Roll ($^\circ$)
$z = z_{GPS}$	1.35	1.77	0.91	12.97	0.26	0.17
$z = [z'_{GPS} z'_m z'_g]^T$	0.65	1.51	0.91	3.16×10^{-3}	0.18	0.14

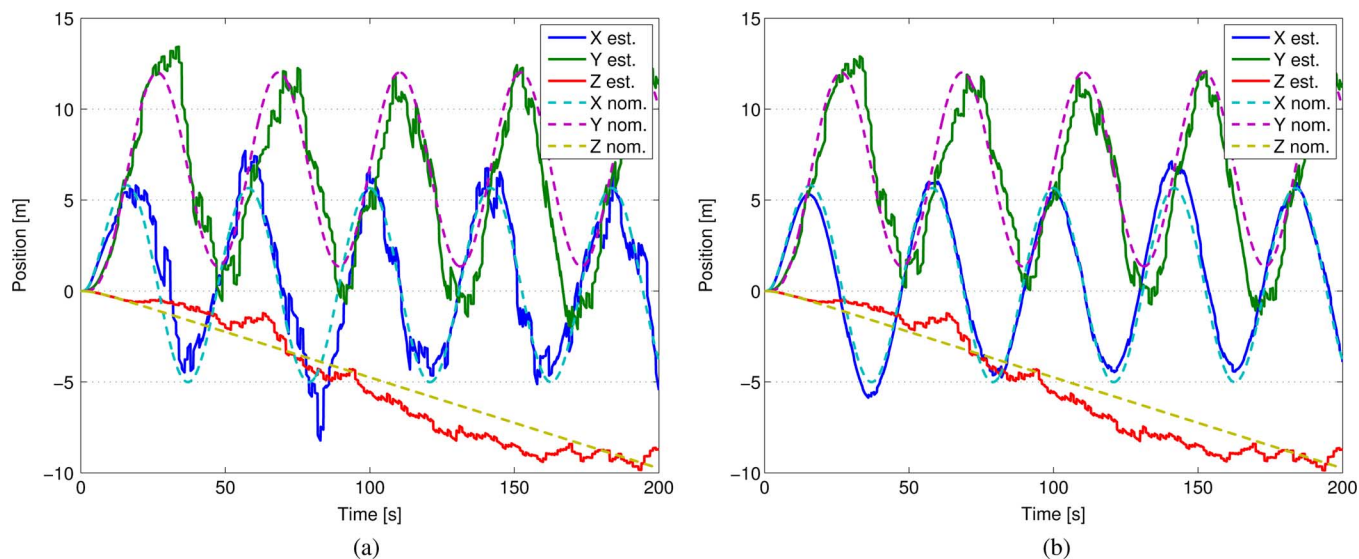


Fig. 8. Trimming trajectory results: the x- and y-axes position estimation is enhanced by the magnetic and pendular readings. The z-axis position estimate is not influenced by the vector readings, since the trimming trajectory does not yield a correlation between attitude and z-axis position errors. (a) GPS aiding only. (b) GPS, magnetic and pendular aiding.

is installed that can carry acoustic transducers. For bathymetric operations and seafloor characterization, the wing can be equipped with a Tritech Super SeaKing mechanically scanned pencil beam sonar or a RESON 8125 multibeam sonar. A SICK LD-LRS3100 laser range finder is installed on top of this structure. It is used to survey the emerged part of semi-submerged infra-structures like breakwaters.

The DELFIMx hardware architecture developed by the ISR-IST is a self-contained system mounted on three cases which can be fit into and removed from the ASC. The most sensitive parts are vibration isolated from the hull using a soft suspension mechanism, which acts as a lowpass mechanical filter that provides further attenuation of the ASC vibration on the electronics. The hardware architecture is built around

TABLE III
 FILTER RESULTS, TRIMMING TRAJECTORY

	Root Mean Square (RMS) Error					
	p_x (m)	p_y (m)	p_z (m)	Yaw ($^\circ$)	Pitch ($^\circ$)	Roll ($^\circ$)
$\mathbf{z} = \mathbf{z}_{\text{GPS}}$	1.35	1.77	0.91	12.96	0.26	0.17
$\mathbf{z} = \begin{bmatrix} \mathbf{z}'_{\text{GPS}} & \mathbf{z}'_m \end{bmatrix}'$	0.66	1.79	0.91	3.17×10^{-3}	0.20	0.17
$\mathbf{z} = \begin{bmatrix} \mathbf{z}'_{\text{GPS}} & \mathbf{z}'_m & \mathbf{z}'_g \end{bmatrix}'$	0.65	1.51	0.91	3.16×10^{-3}	0.18	0.14

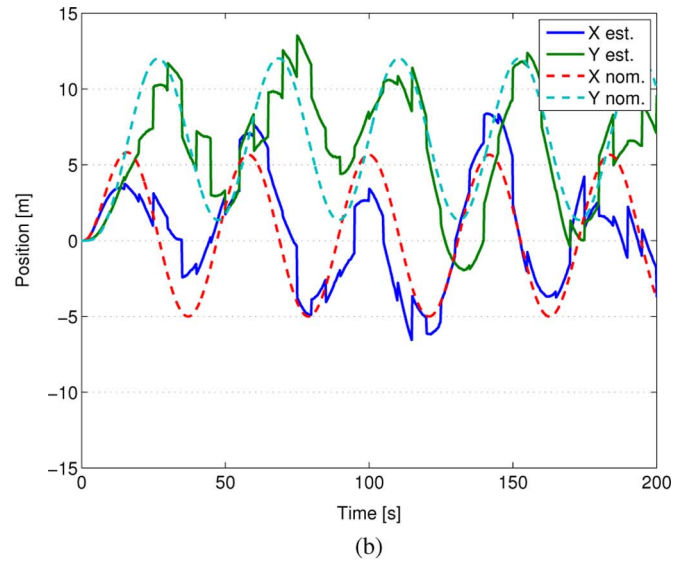
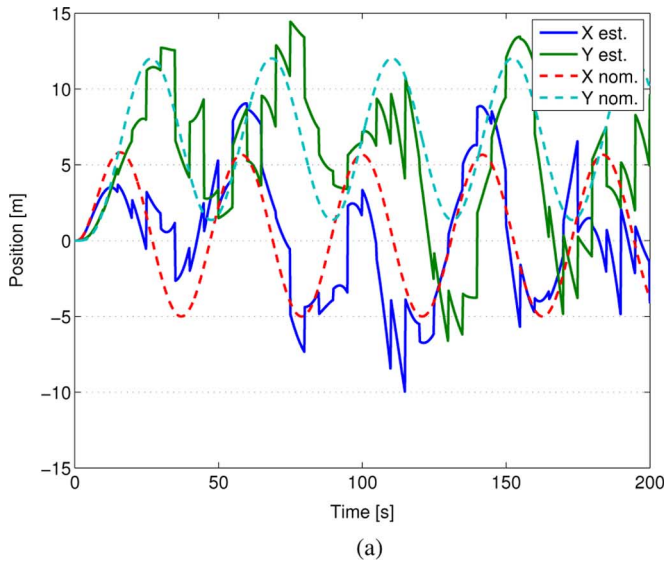


Fig. 9. Position results for GPS signal with low sampling rate (0.2 Hz): the pendular readings reduce the drift of the position estimates between GPS samples. (a) GPS aiding only. (b) GPS and gravity aiding.

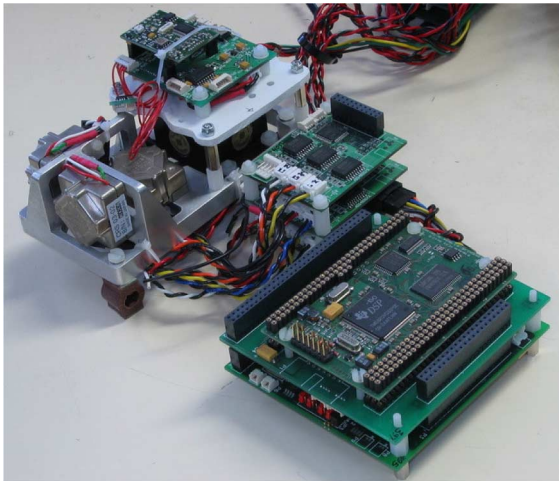


Fig. 10. Hardware installed onboard the DELFIMx ASC: the hardware architecture is built around the DSP TI TMS320C33, and the IMU comprises a tri-axial XBOX CXL02LF3 accelerometer and three single axes Silicon Sensing CRS03 rate gyros.

the low-cost low-power floating point DSP TI TMS320C33, displayed in Fig. 10, which is connected to the data acquisition hardware through a dual port RAM expansion board developed by IST-ISR. Special care was taken during the electronics development to implement measures that improve the electromagnetic compatibility (EMC). The data acquisition

distributed architecture was built around the CAN (controller area network) industrial real time network, for control and navigation purposes and on 100 Mb/s ethernet for payload data interface. A series of very low-power boards designed at ISR using the Phillips XAS3 16-bit microcontroller, and the ATMEL AT90CAN128 8-bit AVR® flash microcontroller with extended CAN capabilities are used to interface all sensors and exchange data through the CAN Bus. In this architecture the TMS320C33 schedules all guidance, control, and navigation tasks to meet their deadlines. Finally, a PC104 board connected to the CAN Bus and to ethernet runs the mission control system and implements a blackbox where relevant data generated by the ASC are properly saved in a solid-state disk for postmission analysis.

The inertial measurement unit (IMU) on-board the DELFIMx craft is a strapdown system comprising a triaxial XBOX CXL02LF3 accelerometer and three single axes Silicon Sensing CRS03 rate gyros mounted along three orthogonal axes. These sensors are attached orthogonally to a custom made stand, that is presented in Fig. 10 with the sensors assembled. The inertial sensors are sampled at 56 Hz using six Texas ADS1210 directly connected to a microcontroller board. The ADS1210 is a high precision, wide dynamic range, delta-sigma analog-to-digital converter with 24-bit resolution operating from a single +5 V supply. The differential inputs are ideal for direct connection to transducers guaranteeing 20 bits of effective resolution which is a suitable accuracy for the set of inertial sensors used in the present application.

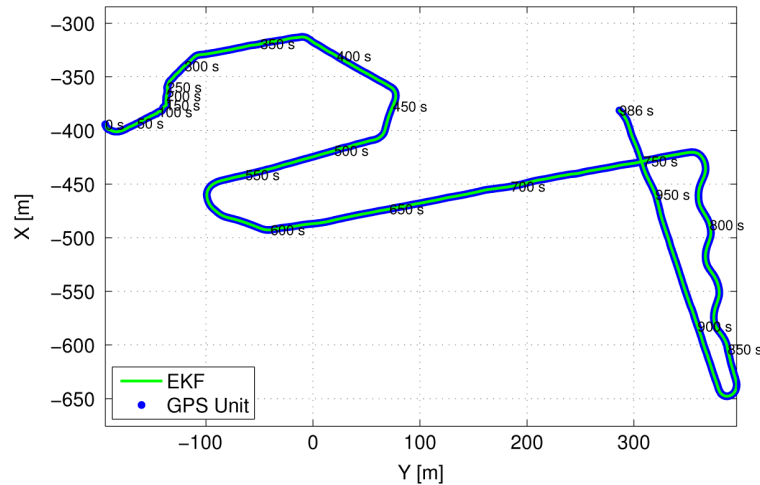


Fig. 11. Measured and estimated DELFIMx trajectory: the position estimate is consistent with the GPS readings obtained along the mission.

The hardware architecture is also equipped with a Honeywell HMR3300 magnetometer, interfaced by a serial port connection with a sampling rate of 8 Hz. The GPS receiver installed on board the DELFIMx is a Thales Navigation DG14 receiver which presents an accuracy of 3.0 m circular error probable (CEP) in autonomous mode and 0.40 m in differential mode. In the present work, the GPS works in autonomous mode and the measurements are provided at a 4 Hz sampling rate. The diverse frequency rates of the aiding sensors, i.e., GPS, magnetometer, and pendular measurement, are easily handled in the filter by selecting the rows of the measurement matrix (17) according to the available measurement at each time instant.

B. Experimental Results Analysis

This section evaluates the navigation system for a set of experimental data. The results presented in this work were obtained for a DELFIMx seatrial conducted on October 2007 off the coast of Sesimbra, Portugal, located at $38^{\circ}26' N$, $9^{\circ}6' W$. The trajectory described by the catamaran was obtained using the path-following preview controller proposed in [34], and was designed to demonstrate the maneuverability of the vehicle in challenging applications with straight lines, curves and oscillatory trajectories generated by coning motion, as shown in Fig. 11.

The parameters of the EKF were tuned as follows. The pendular model of \mathbf{g}_r , described in (14) and (15), was characterized by the covariance $\sigma_{LA}^2 = 10^{-5}$ and the poles were obtained by frequency analysis of \mathbf{g}_r for a set of DELFIMx's maneuvers. Due to the ASC's physical characteristics, the component ${}^B\mathbf{g}$ in (14) was modeled as a low frequency signal, while the frequency contents \mathbf{a}_{LA} were shaped in the remaining frequency spectrum. Since the propulsion force of an ASC is physically oriented along the body x -axis, the y -axis is less exposed to linear acceleration and the spectrogram of g_{ry} and g_{rz} can be studied to identify the low-frequency region associated with ${}^B\mathbf{g}$. This tuning procedure showed that the low frequency contents of ${}^B\mathbf{g}$ vanished at $\alpha_l = 3.64$ Hz, and that \mathbf{a}_{LA} was a high-frequency process, hence modeled by setting the second cutoff pole near the Nyquist frequency of the system, $\alpha_h = 27$ Hz.

The covariances of the inertial and aiding sensors were computed by processing sensor data obtained with the DELFIMx at rest in the harbor facilities. The classical technique of improving the system robustness by inflating the noise covariances was adopted [35], namely the covariance of the pendular observation noise \mathbf{n}_g was defined as $\Xi_g = 10^{-5}\mathbf{I}_3$ to account for second-order terms in the observation model (16), and the velocity error state covariance was set as $\Xi_v = \Xi_a + 7 \times 10^{-4}\mathbf{I}_3$, to balance the influence of the GPS aiding and the IMU computations in the estimated position and velocity. To validate the adopted covariances, it will be shown that the navigation system successfully merges the available information and is in fact robust to GPS outage. To better illustrate the qualities of the proposed solution, navigation system results with GPS signal blockage are also considered in this section.

The navigation system was initialized using attitude and position estimates provided by the aiding sensors. The initial attitude guess was obtained using the QUEST attitude reconstruction algorithm [7] to process the first magnetometer and accelerometer measurements, and the position estimate was acquired directly from the first good quality GPS measurement available.

The position and attitude estimation results are presented in Figs. 11 and 12, and are consistent with the trajectory outlined by the GPS measurements. The estimated position smoothly tracks the trajectory described by the DELFIMx catamaran, as shown in Fig. 11. The estimated yaw, illustrated in Fig. 12(a), is according to the described trajectory, and to the heading measurement provided by the GPS, which is depicted only for comparison purposes. Also, Fig. 12(a) shows that the adopted architecture based on vector readings yields a yaw estimate that is more smooth and accurate than the yaw estimate given by GPS-based heading systems. The average estimated pitch and roll angles, shown in Fig. 12(b), are according to the installation angles of the IMU architecture in the DELFIMx platform.

The estimated angular and linear velocities of the catamaran are shown in Fig. 13. The angular velocity is consistent with the vehicle maneuvers. The linear velocity is represented in body fixed coordinates because the velocity variations occur naturally in the body axis. As expected, Bv_x is positive and characterized

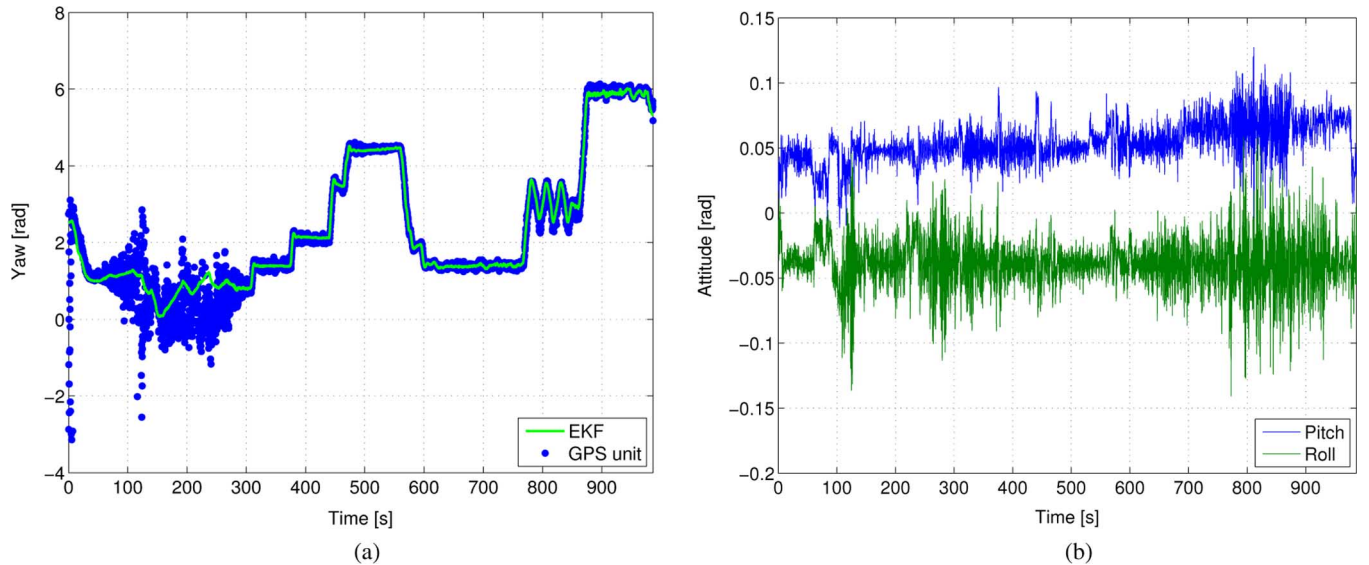


Fig. 12. Attitude estimation results (DELFINx trajectory): (a) the yaw estimate is consistent with the heading measurement provided by the GPS unit, that is depicted only for comparison purposes, (b) the pitch and roll estimates are according to the installation angles of the IMU, and consistent with the maneuvers performed by the ASC. (a) Yaw. (b) Pitch and roll.

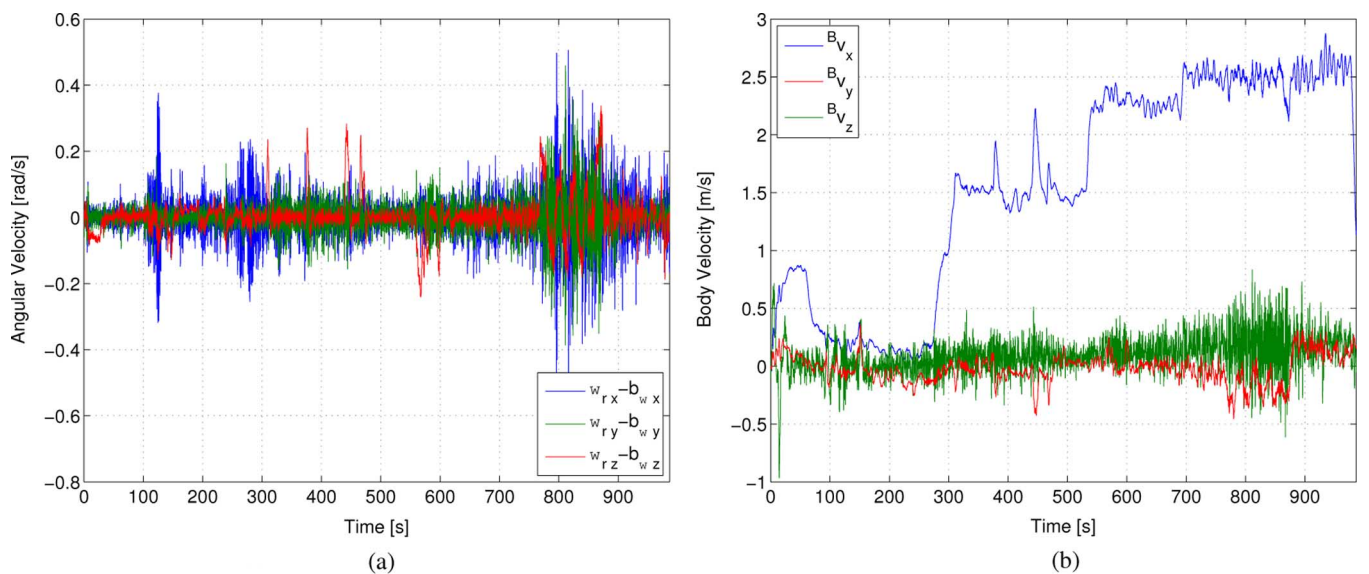


Fig. 13. Velocity estimation results (DELFINx trajectory): the linear and angular velocity estimates are consistent with the trajectory described by the ASC. Namely, angular velocity fluctuates during turning maneuvers, lateral velocities oscillate around zero, and forward velocity is positive in straight line trajectories. (a) Angular velocity. (b) Linear velocity in body frame.

roughly by forward velocities, while the lateral and vertical velocities fluctuate around zero.

Although the navigation system was stable in extensive simulation studies where large initial bias estimation error was considered, offline calibration was adopted in practice to guarantee that the small error assumption of the EKF perturbational model was kept valid from the start. An initial guess of the accelerometer and rate gyro biases was obtained offline and after warming up the IMU. The initial covariance of the filter was set to compensate for small errors of the offline calibration, and to account for the bias fluctuations between the time instants of the calibration procedure and the navigation system initialization. The filter covariances Ξ_{b_a} , Ξ_{b_ω} were designed small enough to

compensate for the slow variations of the bias in the course of the mission, $\Xi_{b_a} = \Xi_{b_\omega} = 10^{-12} \mathbf{I}_3$. The obtained bias estimates were approximately constant, which endorses the slowly varying bias model.

The vector aiding technique described in Section IV was adapted to the application at hand. Analyzing the measurement model (16) for ${}^E \mathbf{g} = [0 \ 0 \ g]'$, it is straightforward to verify that the z-axis measurement residual ${}^E z_{g z}$ does not relate to the attitude error $\delta \boldsymbol{\lambda}$, i.e., it is uninformative for the purpose of attitude determination. Also, the collected magnetometer data were roughly planar and hence enough to calibrate only the soft iron and hard iron distortions in the xy plane of the magnetometer. Consequently, the vertical components of the

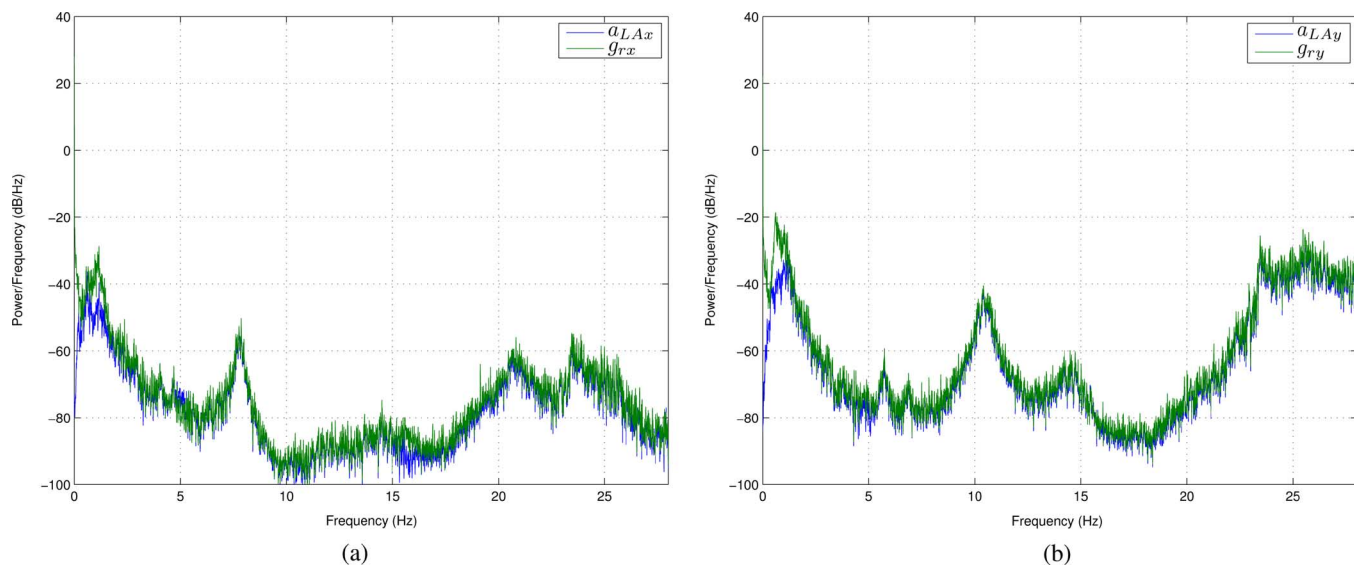


Fig. 14. Frequency contents of the pendular reading and of the estimated linear acceleration: the linear acceleration estimated by filter, denoted as \mathbf{a}_{LA} , is similar to the pendular reading \mathbf{g}_r in the medium and high-frequency regions, as desired. This shows that the filter extracts the low-frequency contents of \mathbf{g}_r to estimate the attitude of the vehicle. (a) Body frame x-axis. (b) Body frame y-axis.

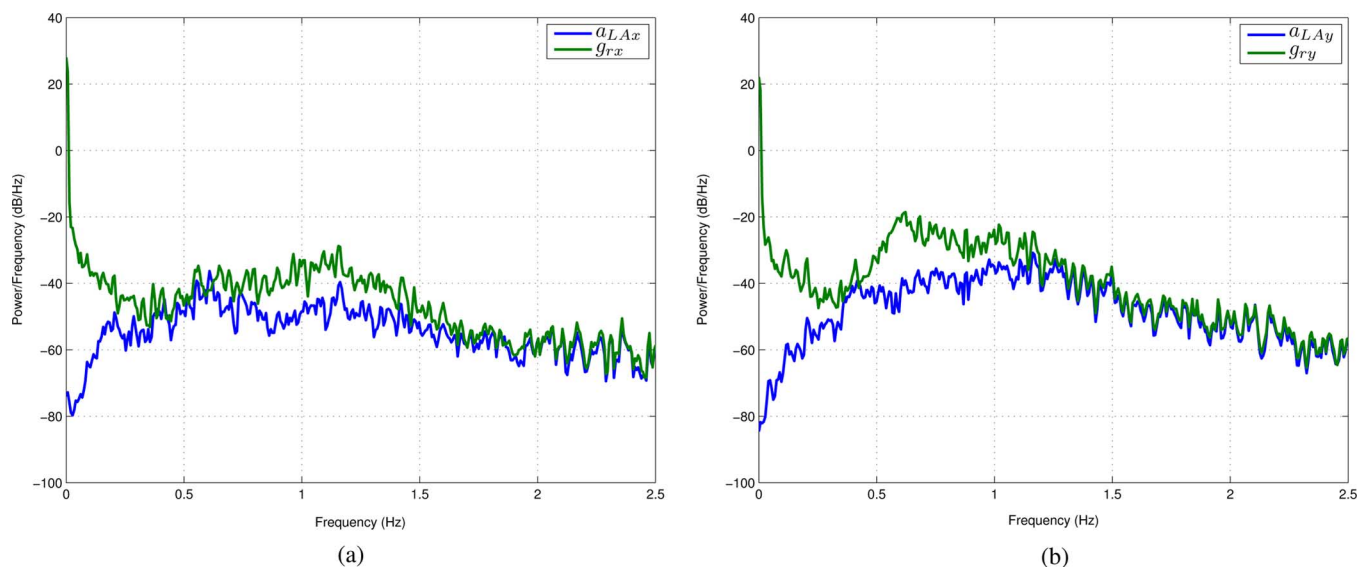


Fig. 15. Frequency contents of the pendular reading and of the estimated linear acceleration (low-frequency region): the information of \mathbf{g}_r contained in the low-frequency region is used by the filter to estimate attitude errors. (a) Body frame x-axis. (b) Body frame y-axis.

measurement residuals $E_{z_{gz}}$ and $E_{z_{mz}}$ were put aside in the course of the filtering algorithm, by omitting the corresponding rows of the measurement matrix \mathbf{H} . The aiding measurements components can be easily selected, which shows the flexibility of the present navigation solution.

The modeling of the pendular vector measurements described in Section IV.B is validated using frequency domain analysis of the measured and estimated signals. The power spectral density (PSD) of the desired signals was obtained using Matlab's `pwelch` function, i.e., Welch's averaged modified periodogram method of spectral approximation. Fig. 14 presents the frequency contents of the pendular reading \mathbf{g}_r , defined in (13), and that of the linear acceleration estimate \mathbf{a}_{LA} , defined in (15). The PSDs of \mathbf{g}_r and \mathbf{a}_{LA} are very similar in the medium and high frequency regions, and diverge in the low frequency

domain where the PSD of \mathbf{a}_{LA} is smaller than the PSD of \mathbf{g}_r . This shows that the filter exploits, in fact, the low-frequency contents of \mathbf{g}_r for attitude estimation, while the medium and high frequency linear acceleration disturbances are associated with the signal \mathbf{a}_{LA} , as desired. The PSD of the signals in the low-frequency region is shown in detail in Fig. 15.

The dependency of the navigation system with respect to the aiding measurements is studied by disabling the GPS measurements at selected time intervals when the vehicle turns or enters in long straight paths. The nominal and estimated trajectories are shown in Fig. 16, and a zoom of the trajectories at the GPS outage time intervals is presented in Fig. 17. The position and attitude estimates track the curve and straight line paths in the short term, which shows that the performance of the system without GPS aiding is adequate for practical applications. It also

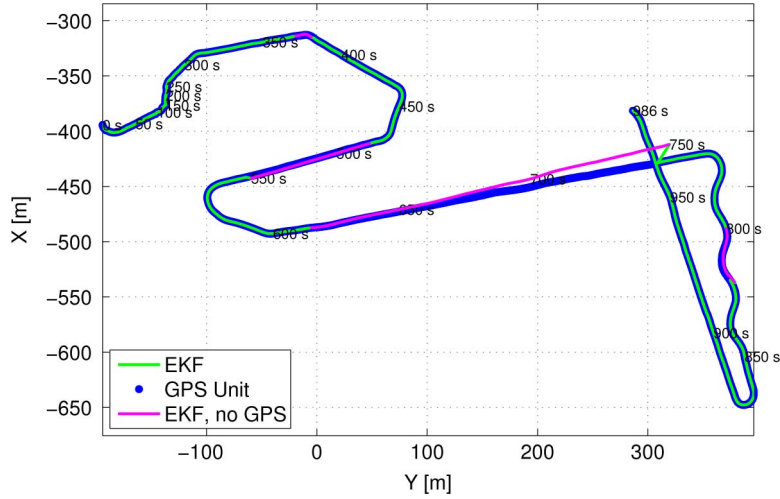


Fig. 16. Measured and estimated DELFIMx trajectories with GPS outage: although the GPS is disabled at $t \in [370\ 380]$ s, $t \in [480\ 550]$ s, $t \in [615\ 750]$ s, and $t \in [800\ 820]$ s, the position estimates track the nominal trajectory.

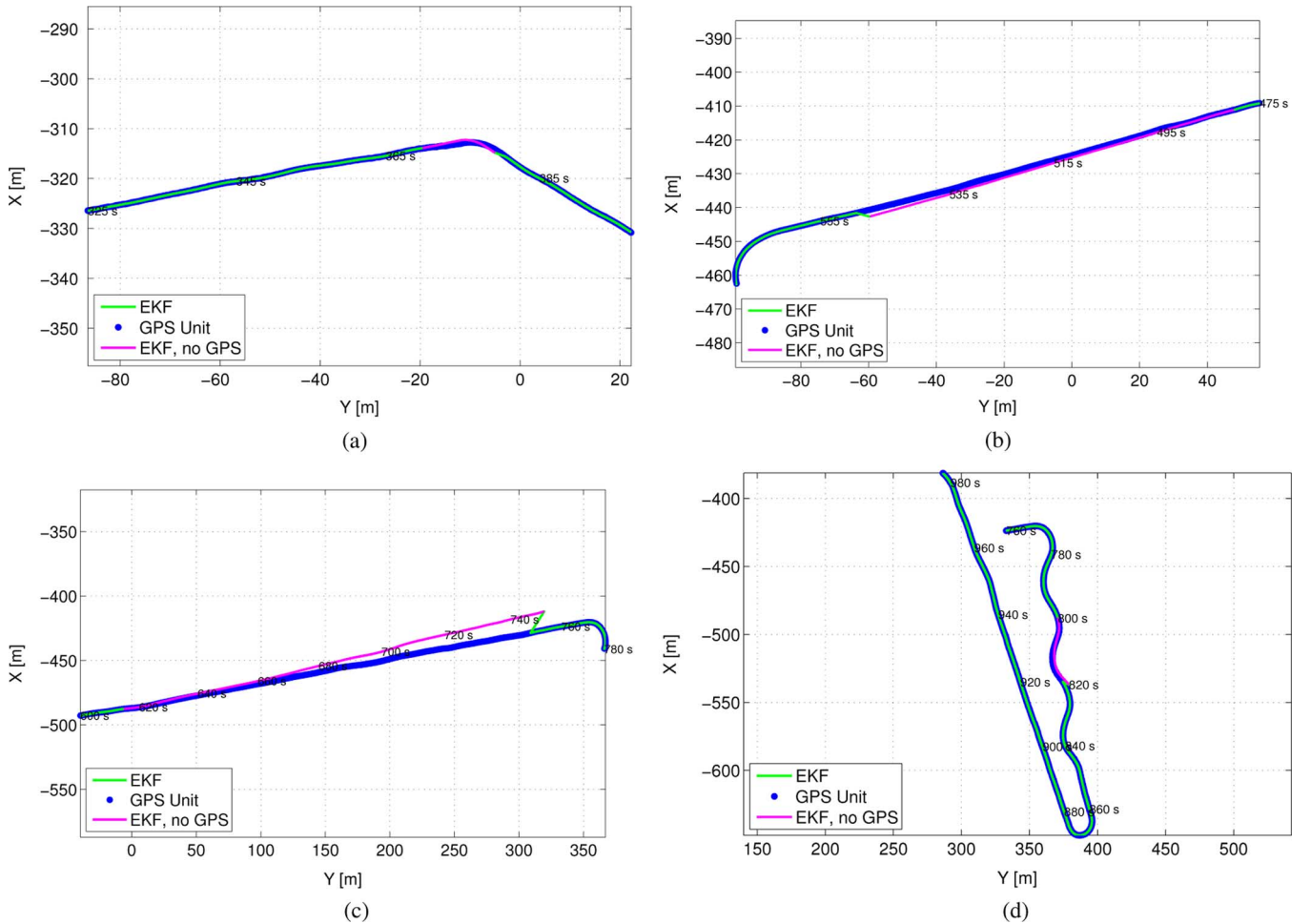


Fig. 17. Estimated and measured positions at the time intervals of the GPS outage: the navigation system errors are bounded even if GPS measurements are unavailable. (a) GPS outage at $[370\ 380]$ s. (b) GPS outage at $[480\ 550]$ s. (c) GPS outage at $[615\ 750]$ s. (d) GPS outage at $[800\ 820]$ s.

demonstrates that the navigation system acts according to the concept of filtering, by merging the IMU and aiding measurements without relying solely on the GPS data.

The tests in the presence of GPS outage also illustrate the necessity of pendular measurements, as shown in Table IV, where the position drift is approximated by the first measurement

residual \mathbf{z}_{GPS} when the GPS is successfully reacquired. The results show that pendular measurements effectively reduce the system drift. Given that the drift's magnitude is a measure of the navigation system accuracy, this case study shows that the performance of the system is enhanced by the pendular measurements.

TABLE IV
GPS OUTAGE RESULTS

Time Interval (s)	With Pendular Aiding		Without Pendular Aiding	
	Final Position Drift (m)	Average Position Drift (m/s)	Final Position Drift (m)	Average Position Drift (m/s)
[370 380]	1.76	0.176	5.65	0.565
[480 550]	4.24	0.061	28.51	0.407
[615 750]	20.3	0.150	720.5	5.337
[800 820]	5.60	0.280	11.96	0.598

VIII. CONCLUSION

An advanced global positioning system/inertial navigation system (GPS/INS) using extended Kalman filter (EKF) and integrating vector observations was described. The navigation system comprised an high-accuracy, multirate inertial integration algorithm, combined with an EKF in a direct-feedback configuration to compensate for inertial sensors nonidealities. An aiding technique that directly integrates vector measurements in the filter was detailed, allowing for the use of a frequency domain model of the vehicle motion in the filter. The experimental results obtained at sea with the DELFIMx ASC showed that the proposed navigation system can accurately estimate position and attitude. The compensation of sensor nonidealities such as bias and noise effects, and the autonomy with respect to GPS aiding by exploiting the vector measurement directly in the filter, were demonstrated in practice.

REFERENCES

- [1] L. Silva, J. Santos, M. Neves, C. Silvestre, P. Oliveira, and A. Pascoal, "Tools for the diagnosis and automated inspection of semisubmerged structures," in *Proc. 13th Int. Harbour Congr.*, Antwerp, Belgium, Mar.–Apr. 2003.
- [2] C. Silvestre, P. Oliveira, A. Pascoal, L. Silva, J. Santos, and M. Neves, "Inspection and diagnosis of the Sines West breakwater," in *Proc. ICCE2004 29th, Int. Conf. Coastal Eng.*, Lisbon, Sep. 2004.
- [3] P. Savage, "Strapdown inertial navigation integration algorithm design part 1: Attitude algorithms," *AIAA J. Guidance, Contr., Dynam.*, vol. 21, no. 1, pp. 19–28, Jan.–Feb. 1998.
- [4] P. Savage, "Strapdown inertial navigation integration algorithm design part 2: Velocity and position algorithms," *AIAA J. Guidance, Contr., Dynam.*, vol. 21, no. 2, pp. 208–221, Mar.–Apr. 1998.
- [5] J. L. Crassidis, F. L. Markley, and Y. Cheng, "Survey of nonlinear attitude estimation methods," *J. Guidance, Contr., Dynam.*, vol. 30, no. 1, pp. 12–28, Jan.–Feb. 2007.
- [6] I. Bar-Itzhack and R. Harman, "Optimized TRIAD algorithm for attitude determination," *J. Guidance, Contr., Dynam.*, vol. 20, no. 1, pp. 208–211, Jan. 1997.
- [7] M. D. Shuster and S. D. Oh, "Three-axis attitude determination from vector observations," *J. Guidance, Contr., Dynam.*, vol. 4, no. 1, pp. 70–77, Jan.–Feb. 1981.
- [8] J. Vasconcelos, P. Oliveira, and C. Silvestre, "Inertial navigation system aided by GPS and selective frequency contents of vector measurements," in *Proc. AIAA Guidance, Navigation, Control Conf. (GNC2005)*, San Francisco, CA, Aug. 2005.
- [9] A. Alcocer, P. Oliveira, and A. Pascoal, "Study and implementation of an EKF GIB-based underwater positioning system," *IFAC J. Contr. Eng. Practice*, vol. 15, no. 6, pp. 689–701, Jun. 2007.
- [10] M. Morgado, C. Silvestre, P. Oliveira, and J. Vasconcelos, "Improving aiding techniques for USBL tightly-coupled inertial navigation system," in *Proc. 17th IFAC World Congress*, Seoul, Korea, Jul. 2008.
- [11] P. Lee, B. Jeon, S. Kim, H. Choi, C. Lee, T. Aoki, and T. Hyakudome, "An integrated navigation system for autonomous underwater vehicles with two range sonars, inertial sensors and Doppler velocity log," in *Proc. OCEANS'04. MTS/IEEE TECHNO-OCEAN'04*, Nov. 2004, vol. 3, pp. 1586–1593.
- [12] D. Steinke and B. Buckham, "A Kalman filter for the navigation of remotely operated vehicles," in *Proc. MTS/IEEE OCEANS, 2005*, Sep. 2005, vol. 1, pp. 581–588.
- [13] O. Hegrenaes, E. Berglund, and O. Hallingstad, "Model-aided inertial navigation for underwater vehicles," in *Proc. 2008 IEEE Int. Conf. Robot. Automation, ICRA 2008*, May 2008, pp. 1069–1076.
- [14] T. I. Fossen, *Guidance and Control of Ocean Vehicles*. New York: Wiley, 1994.
- [15] T. I. Fossen, S. I. Sagatun, and A. J. Srensen, "Identification of dynamically positioned ships," *J. Contr. Eng. Practice*, vol. 4, no. 3, pp. 369–376, Mar. 1996.
- [16] J. C. Kinsey, R. M. Eustice, and L. L. Whitcomb, "A survey of underwater vehicle navigation: Recent advances and new challenges," in *Proc. 7th IFAC Conf. Manoeuvring Contr. of Marine Craft (MCMC)*, Lisbon, Portugal, Sep. 2006, (Invited Paper).
- [17] F. Markley, "Attitude error representations for Kalman filtering," *AIAA J. Guidance, Contr., Dynam.*, vol. 26, no. 2, pp. 311–317, Mar.–Apr. 2003.
- [18] K. Britting, *Inertial Navigation Systems Analysis*. New York: Wiley, 1971.
- [19] M. Pittelkau, "Rotation vector in attitude estimation," *AIAA J. Guidance, Contr., Dynam.*, vol. 26, no. 6, pp. 855–860, Nov.–Dec. 2003.
- [20] J. Bortz, "A new mathematical formulation for strapdown inertial navigation," *IEEE Trans. Aerospace Electron. Syst.*, vol. 7, no. 1, pp. 61–66, Jan. 1971.
- [21] K. Roscoe, "Equivalency between strapdown inertial navigation coning and sculling integrals/algorithms," *AIAA J. Guidance, Contr., Dynam.*, vol. 24, no. 2, pp. 201–205, Mar.–Apr. 2001.
- [22] P. Savage, *Strapdown Analytics*. Maple Plain, MN: Strapdown Associates, Inc., 2000, vol. 1.
- [23] D. Goshen-Meskin and I. Bar-Itzhack, "Observability analysis of piece-wise constant systems—Part II: Application to inertial navigation in-flight alignment," *IEEE Trans. Aerospace Electron. Syst.*, vol. 28, no. 4, pp. 1068–1075, Oct. 1992.
- [24] J. Vasconcelos, C. Silvestre, and P. Oliveira, "Embedded vehicle dynamics and laser aiding techniques for inertial navigation systems," in *Proc. AIAA Guidance, Navigation, Contr. Conf. (GNC2006)*, Keystone, CO, USA, Aug. 2006.
- [25] X. Ma, S. Sukkarieh, and J. Kim, "Vehicle model aided inertial navigation," in *Proc. IEEE Intelligent Transportation Syst.*, Shanghai, China, Oct. 2003, vol. 2, pp. 1004–1009.
- [26] M. Koifman and I. Bar-Itzhack, "Inertial navigation system aided by aircraft dynamics," *IEEE Trans. Control Syst. Technol.*, vol. 7, no. 4, pp. 487–493, Jul. 1999.
- [27] J. Vasconcelos, J. Calvário, P. Oliveira, and C. Silvestre, "GPS aided imu for unmanned air vehicles," in *Proc. 5th IFAC/EURON Symp. Intelligent Autonomous Vehicles (IAV2004)*, Lisbon, Portugal, Jul. 2004.
- [28] G. Wahba, "A least-squares estimate of satellite attitude," *SIAM Rev.*, vol. 7, no. 3, p. 409, 1965, problem 65-1.
- [29] R. Alonso and M. D. Shuster, "Complete linear attitude-independent magnetometer calibration," *The J. Astronautical Sci.*, vol. 50, no. 4, pp. 477–490, Oct.–Dec. 2002.
- [30] C. C. Foster and G. H. Elkaim, "Extension of a non-linear, two-step calibration methodology to include non-orthogonal sensor axes," *IEEE J. Aerospace Electron. Syst.*, vol. 44, no. 3, pp. 1070–1078, Jul. 2008.
- [31] R. Brown and P. Hwang, *Introduction to Random Signals and Applied Kalman Filtering*, 3rd ed. New York: Wiley, 1997.
- [32] A. Gelb, *Applied Optimal Estimation*. Cambridge, MA: MIT Press, 1974.
- [33] P. Gomes, C. Silvestre, A. Pascoal, and R. Cunha, "A coastline following preview controller for the DELFIMx vehicle," in *Proc. 17th Int. Offshore Polar Eng. Conf. Exhib.*, Lisbon, Portugal, Jul. 2007.
- [34] P. Gomes, C. Silvestre, A. Pascoal, and R. Cunha, "A path-following controller for the delfimx autonomous surface craft," in *Proc. 7th IFAC Conf. Manoeuvring Contr. Marine Craft (MCMC)*, Lisbon, Portugal, Sep. 2006.
- [35] B. D. O. Anderson and J. B. Moore, *Optimal Filtering*. New York: Dover, 1979.



José F. Vasconcelos (M'09) received the Licenciatura and the Ph.D. degrees in electrical engineering from the Instituto Superior Técnico (IST), Lisbon, Portugal, in 2003 and 2010, respectively.

Since 2009, he has been a Project Engineer with the Advanced Projects Department, Deimos Engenharia, Lisbon, Portugal. His research interests include nonlinear observers, inertial navigation systems, sensor calibration, and robust control with application to autonomous vehicles.



Carlos Silvestre (M'07) received the Licenciatura degree in electrical engineering and the M.Sc. degree in electrical engineering and the Ph.D. degree in control science from the Instituto Superior Técnico (IST), Lisbon, Portugal, in 1987, 1991 and 2000, respectively.

Since 2000, he has been with the Department of Electrical Engineering, IST, where he is currently an Associate Professor of Control and Robotics. Over the past years, he has conducted research in the fields of guidance, navigation, and control of air and under-

water robots. His research interests include linear and nonlinear control theory, coordinated control of multiple vehicles, gain scheduled control, integrated design of guidance and control systems, inertial navigation systems, and mission control and real time architectures for complex autonomous systems with applications to unmanned air and underwater vehicles.



Paulo Oliveira (S'91–M'95) received the Licenciatura, M.Sc., and Ph.D. degrees in electrical and computer engineering in 1987, 1991, and 2002, respectively, from Instituto Superior Técnico (IST), Lisbon, Portugal.

He is an Associate Professor in the Department of Mechanical Engineering of IST and a Senior Researcher in the Institute for Systems and Robotics–Associated Laboratory. His research interests are in the area of autonomous robotic vehicles with focus on the fields of estimation, sensor fusion, navigation, positioning, and industrial automation. He is author or coauthor of more than 20 journal papers and 100 conference communications. He has participated in more than 20 European and Portuguese research projects, over the last 25 years.